



Norwegian University of  
Science and Technology

# Aerodynamics of an airfoil subjected to icing

**Magnus Kyrkjebø**

Master of Science in Mechanical Engineering

Submission date: June 2018

Supervisor: Robert Jason Hearst, EPT

Norwegian University of Science and Technology  
Department of Energy and Process Engineering



EPT-M-2018-52

**MASTER THESIS**

for

Magnus Kyrkjebø Vinnes

Spring 2018

Aerodynamics of an airfoil subjected to icing

*Aerodynamikken til en vinge med isdannelse***Background and objective**

Atmospheric icing on aircraft is known to degrade aerodynamic performance by increasing drag and decreasing lift. While icing has been extensively studied for commercial and military aircraft, surprisingly little research has been performed at low Reynolds numbers, where wind turbines and unmanned aerial vehicles (UAVs) operate. To understand the mechanisms by which icing impacts lift and drag, artificial ice will be attached to an airfoil in a wind tunnel, and the flow physics will be measured with particle image velocimetry (PIV) or laser-Doppler anemometry (LDA). Three different icing conditions will be compared to the no icing condition at multiple angles-of-attack. The overall object of the work is to identify the impact of the icing geometry on lift and stall by comparing the measured flow fields to previously acquired force measurements.

**The following tasks are to be considered:**

- 1) Detailed literature review on airfoil icing as well as PIV/LDA of airfoils.
- 2) Construction of experimental apparatus to house the measurement equipment.
- 3) Complete necessary safety training and risk assessments.
- 4) Test and learn to operate measurement equipment before experimental campaign.
- 5) Perform measurements of the airfoil with four icing geometries at a minimum of 3 angles-of-attack.
- 6) Process data to extract mean and variance/velocity fluctuation information.
- 7) Compare experimental flow measurements to previously conducted force measurements and CFD.

-- ” --

Within 14 days of receiving the written text on the master thesis, the candidate shall submit a research plan for his project to the department.

When the thesis is evaluated, emphasis is put on processing of the results, and that they are presented in tabular and/or graphic form in a clear manner, and that they are analyzed carefully.

The thesis should be formulated as a research report with summary both in English and Norwegian, conclusion, literature references, table of contents etc. During the preparation of the text, the candidate should make an effort to produce a well-structured and easily readable report. In order to ease the evaluation of the thesis, it is important that the cross-references are correct. In the making of the report, strong emphasis should be placed on both a thorough discussion of the results and an orderly presentation.

The candidate is requested to initiate and keep close contact with his/her academic supervisor(s) throughout the working period. The candidate must follow the rules and regulations of NTNU as well as passive directions given by the Department of Energy and Process Engineering.

Risk assessment of the candidate's work shall be carried out according to the department's procedures. The risk assessment must be documented and included as part of the final report. Events related to the candidate's work adversely affecting the health, safety or security, must be documented and included as part of the final report. If the documentation on risk assessment represents a large number of pages, the full version is to be submitted electronically to the supervisor and an excerpt is included in the report.

Pursuant to "Regulations concerning the supplementary provisions to the technology study program/Master of Science" at NTNU §20, the Department reserves the permission to utilize all the results and data for teaching and research purposes as well as in future publications.

The final report is to be submitted digitally in DAIM. An executive summary of the thesis including title, student's name, supervisor's name, year, department name, and NTNU's logo and name, shall be submitted to the department as a separate pdf file. Based on an agreement with the supervisor, the final report and other material and documents may be given to the supervisor in digital format.

- Work to be done in lab (Water power lab, Fluids engineering lab, Thermal engineering lab)  
 Field work

Department of Energy and Process Engineering, 9. January 2018



---

Prof. R. Jason Hearst  
Academic Supervisor





## Abstract

Wind turbines located in cold climate face several issues due to ice accretion. These include power losses, mechanical failures and changes in the aerodynamic behaviour. Particle image velocimetry measurements have been performed on a NREL S826 airfoil subjected to three different ice accretions. The ice accretions represent different atmospheric icing conditions, including rime, glaze and mixed conditions. The measurements have been done on a range of angle of attack between  $-4^\circ$  to  $16^\circ$ . The mean flow field, turbulent kinetic energy, mean vorticity and instantaneous swirl are reported for all cases. In addition, proper orthogonal decomposition was performed to identify high energy modes, and to investigate the possibility of controlling the flow based on a limited number of modes.

## Sammendrag

Isdannelse på vindmøller er en utfordring i kalde klimatiske områder. Noen av problemene som kan oppstå er redusert energiproduksjon, utmattelse av komponenter og endret aerodynamisk oppførsel. Ved hjelp av målemetoden particle image velocimetry har strømmingen over en NREL S826 vingeseksjon med isdannelse blitt kartlagt. Tre forskjellige isgeometrier har blitt undersøkt, i tillegg til vingeprofilen uten isdannelse, og eksperimentene er gjort for angrepsvinkler mellom  $-4^\circ$  og  $16^\circ$ . Gjennomsnittshastighet, momentan hastighet, turbulent kinetisk energi, rotasjon og virvling i strømmingen blir presentert. I tillegg har proper orthogonal decomposition blitt brukt for å indentifisere moduser med høyt energiinnhold, og for å se på mulighetene for å styre strømmingen basert på et begrenset antall moduser.





# Preface

I first got the opportunity to work on this project half a year ago. My experience on experimental work was very limited, although my studies so far have provided me with solid knowledge in fluid mechanics in general. I felt mixture of fear for not being able to perform proper experiments and excitement for the possibility to learn something new and work with an interesting project. It has been a journey of much learning and I feel proud sitting with the final result in front of me. It is written as a scientific paper with the purpose of publishing in a journal.

Luckily for me, my supervisor R. Jason Hearst has been very capable of guiding me through all aspects of the experimental work. He has also been of great help navigating me through which results are interesting, and the interpretation of them. This thesis would have been nothing without him. Also, Leon Li was of great help when experiments were performed.

I hope you will enjoy your reading.

*Trondheim, 07.06.18*

*Magnus Kyrkjebø Vinnes*



# Contents

<b>1</b>	<b>Introduction</b>	<b>1</b>
<b>2</b>	<b>Experimental procedure</b>	<b>5</b>
2.1	Experimental setup . . . . .	5
2.2	Data acquisition . . . . .	7
2.3	Processing . . . . .	9
<b>3</b>	<b>Results</b>	<b>10</b>
3.1	Mean flow . . . . .	11
3.2	Turbulent kinetic energy . . . . .	15
3.3	Vorticity . . . . .	18
<b>4</b>	<b>POD analysis</b>	<b>21</b>
4.1	POD analysis . . . . .	21
4.2	Energy of modes . . . . .	24
4.3	POD modes for $AoA = 16^\circ$ . . . . .	25
4.4	Reconstruction of flow . . . . .	25
<b>5</b>	<b>Conclusion</b>	<b>30</b>
	<b>References</b>	<b>31</b>
	<b>Appendix A Experimental setup</b>	<b>35</b>
A.1	Design of specific experimental equipment . . . . .	35
A.1.1	Camera box . . . . .	35
A.1.2	Laser shade . . . . .	36
A.2	Choosing field of view . . . . .	36
A.3	Measurement plane . . . . .	37
	<b>Appendix B Selecting filter window size</b>	<b>40</b>
	<b>Appendix C Risk assessment</b>	<b>41</b>



# Abstract

Wind turbines located in cold climate face several issues due to ice accretion. These include power losses, mechanical failures and changes in the aerodynamic behaviour. Particle image velocimetry measurements have been performed on a NREL S826 airfoil subjected to three different ice accretions. The ice accretions represent different atmospheric icing conditions, including rime, glaze and mixed conditions. The measurements have been done on a range of angle of attack between  $-4^\circ$  to  $16^\circ$ . The mean flow field, turbulent kinetic energy, mean vorticity and instantaneous swirl are reported for all cases. In addition, proper orthogonal decomposition was performed to identify high energy modes, and to investigate the possibility of controlling the flow based on a limited number of modes.

## 1 Introduction

The global wind energy industry is expanding, with over 50 GW added capacity installed yearly between 2014 and 2016 [1]. There is significant interest to expand wind farms into colder climates, particularly in areas that do not have other practical uses. However, in such regions icing atmospheric conditions will occur, causing ice accretion on the airfoils. Parent & Ilinca [2] list several challenges with such icing phenomena on wind turbines, including measurement errors due to ice accretion on sensors, power losses, mechanical failures due to increased loads and changes in material properties, electrical failure and safety hazard if pieces of ice are thrown off the turbine.

Several studies have reported reduced energy production due to icing. For example, a three bladed wind turbine, located on the Acqua Spruzza test site in central Italy, had a reduction of energy production of 12% and 19% during two test years in the mid 90s [3]. To maintain the rotation of a vertical axis rotating rig, it has been shown that the torque requirement increased 70% under severe icing conditions [4].

There are three main categories of atmospheric icing conditions, rime, glaze and mixed icing conditions [4, 5]. *Rime ice* is formed when the temperature is at  $10^\circ\text{C}$  or below. The water droplets then freeze immediately after impinging the airfoil. *Glaze ice* is formed when the temperature is close to  $0^\circ\text{C}$ . The water droplets typically travel some distance along the airfoil surface before freezing. *Mixed ice* is formed in the temperature region between glaze and rime icing conditions. For this condition, some water droplets freeze immediately after impingement, while some travel along the airfoil surface.

Glaze and mixed ice are often more extensive than rime ice, and has a more severe impact on the airfoil aerodynamics. Furthermore, as water droplets travel both in chordwise and spanwise direction, glaze ice geometries tend to be more extensive on the outer part of the turbine span [4]. The formation of ice accretion is also dependent on several other factors, including chord length, angle of attack (AoA), relative wind speed, humidity, properties of the water droplets, duration of atmospheric icing conditions and the airfoil geometry [6–8].

Another way to classify icing on airfoils was presented by Bragg et al. [9]. They stated that for aerodynamical purposes, it is better to classify icing from their geometries rather than the conditions that generate them. They categorised icing into four different geometries. *Roughness* is small ice particles changing the surface roughness at the leading edge. The roughness height is usually larger than the local boundary layer thickness. The next geometry is *horn ice*, where one or two horn shapes protrude from the leading edge, with an angle from the chord. This geometry will usually have most impact on the aerodynamical performance of the airfoil. *Streamwise* icing geometries are more aerodynamically shaped. They consist of a layer of ice around the leading edge. In some cases, streamwise ice might grow into a horn protruding straight from the leading edge. The last geometry, *streamwise-ridge* icing, happens downstream of the leading edge, and appears like feathers from the airfoil. Typically, water droplets travel from the leading edge, where heating elements are installed, and freeze when they reach the end of the heating element. For mixed icing conditions, experimental results show possible generation of ice feathers downstream of the leading edge. They are not necessarily seen in simulations [8].

Regardless of the categorisation methodology, the various types of icing affect the flow field differently. The most extensive icing cases, typically observed for glaze and mixed icing types, have horn like geometries [4]. For these accretions, the ice shape geometry determines the flow, and separation is typically located at the ice horn for all AoA. This generally lead to thin airfoil type stall [10]. Thin airfoil stall is characterised by a separation bubble starting at the leading edge, which expands with increasing AoA until the flow is unable to reattach [11, 12]. Surface roughness of the ice has a larger effect on the flow for streamlined ice accretions. The roughness mostly affects the drag, but also moves the point of turbulent transition farther upstream, due to increased turbulence production near the leading edge [10]. This is typical behaviour for trailing edge stall, where the separation point moves from the trailing edge towards the leading edge with increasing AoA [11, 12].

Hochart et al. [13] investigated lift and drag on wind turbine blades at three different radial cross sections, for rime and glaze icing events. The increase in drag and lift reduction was much higher at the outermost parts of the blade. At

this location, lift decreased with approximately 30% for both icing cases, and drag increased by a factor of roughly 3.1 for the glaze icing and 2.8 for rime icing. This is in accordance with results reported by Barber et al. [14], who found that only ice on the outboard 25% of the span has significant impact on the performance of the turbine. Icing on the outermost 5% of the span actually has equal impact on performance as icing on the inner 75-95% [14]. In addition, larger wind turbines experience smaller decrease in torque than small wind turbines under icing conditions [15].

Several experiments have been performed to measure the forces acting on an airfoil subjected to icing, e.g. [7, 8, 16, 17]. The pressure distribution of the flow has also been evaluated for various icing geometries [17, 18]. Increased drag and reduced lift are observed in most studies. The magnitude of these parameters are dependent on the geometry of the icing profile, the airfoil, Reynolds number (Re) and AoA. Krøgenes et al. [17] performed studies on a NREL S826 airfoil. Their results are shown in Fig. 1. They found that a horn icing geometry (mixed case) reduced stall AoA by  $5^\circ$ . This agrees with results reported by DeGregorio et al. [16]. The lift, for AoA just below stall, decreased by 10% while drag increased by 340%. For the relatively more aerodynamically shaped rime and glaze ice accretions, lift was reduced by approximately 10% and drag was increased by about 80% in the typical operating region.

According to Etemaddar et al. [7], the increase in drag is higher than the reduction in lift, so the reduced performance of wind turbines is mostly due to increased drag. This agrees with the results presented above. The relative difference is smaller for high AoA, where the reduction in lift is more prominent [7]. Some studies report increased performance of the airfoil for some icing cases at high AoA. It has been suggested that in such cases the icing acts as a leading edge slat [4, 19, 20].

The increase in drag is higher when three dimensional icing is investigated [8]. This is explained by the vortices induced in more than one plane. With a three dimensional ice structure, the flow will be divided into cells in the spanwise direction [21, 22]. Inside each cell the flow is two dimensional. When seen from above, the flow inside a cell might have an angle compared to the incoming velocity. Still, the separation bubble behaves in the same manner as for two dimensional ice accretion. In the interface between the cells, the reattachment points moves farther upstream, and the height of the separation bubble is reduced. In this region, the flow is observed to be three dimensional in nature [21, 22]. Nevertheless, because the flow is two dimensional in each cell, a two dimensional icing profile can provide on the mechanics of an iced airfoil.

Particle image velocimetry (PIV) is an attractive tool to investigate separation and unsteady flow fields [23]. Several recent studies have used this technique to

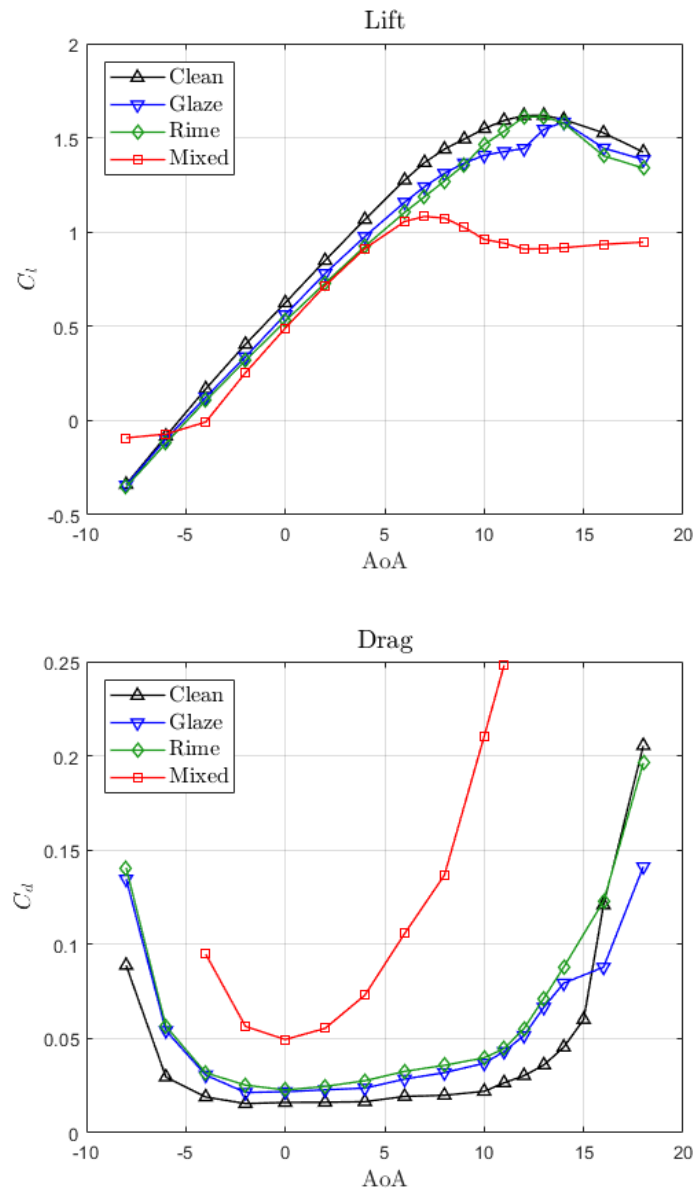


Figure 1: Lift and drag coefficients obtained by Krøgenes et al. [17] for a NREL S826 airfoil with different ice accretions.



investigate the laminar separation bubble (LSB) on low Re airfoils [24–26]. The separation bubble on an iced airfoil has several similarities with a LSB [27]. Using proper orthogonal decomposition (POD), Lengani et al. [28] showed existence of vortex shedding behind the top of a LSB for low Re. For low Re flows, it has also been shown that the reattachment point moves farther upstream with increasing turbulence intensity and Re [25, 29]. The flow over an airfoil subjected to horn icing is similar to a backward facing step flow. For a backward facing step, the reattachment length increases with Re, in contrast to what is observed for the LSB [30], thus expectations for this particular icing geometry differ from simpler geometries.

Jacobs and Bragg [21, 22] performed PIV investigations on a NACA 0012 airfoil with horn ice accretion, at Re about  $9.0 \times 10^5$  and AoA ranging from  $0^\circ$  to  $5^\circ$ . They focused on the separation bubble and reattachment length. Their experiments showed two recirculating zones, one large with clockwise rotation and one small with counter clockwise rotation close to the horn ice geometry. The shear layer between the separation bubble and the freestream flow was also described. It is thin close to the ice horn, and thickens toward the reattachment point [21, 22]. The reattachment point of a separation bubble is unstable [31–33], which explains the wide region of shear stress close to the airfoil. It has also been reported that the flow inside the separation bubble is dominated by vortices [18].

Previous studies focusing flow measurements over an iced airfoil were related to aircraft airfoils or symmetric airfoils. They have also mostly been performed for a limited range of AoA, and most studies only looked at one ice accretion. Therefore, the aim of this work is to investigate the flow over an airfoil designed for wind turbines, with icing profiles attached to the leading edge. Measurements were performed with PIV because it provides adequate spatial resolution to capture the large scale phenomena and it enables observation of complete instantaneous flow fields. A comparison of the flow field for several icing geometries and for AoA ranging from  $-4^\circ$  to  $16^\circ$  has been made. This is followed by a commentary on the vorticity and instantaneous structure in the flow as well as POD analysis. All results are compared to the force measurements of Krøgenes et al. [17], who used the same setup.

## 2 Experimental procedure

### 2.1 Experimental setup

The closed-loop low-speed wind tunnel located at the Norwegian University of Science and Technology (NTNU) was employed for this experimental campaign. The test section in the wind tunnel is 12m long, and has a cross section of 1.8m

Table 1: Surface roughness of icing.

<b>Icing</b>	<b>Roughness [mm]</b>
Glaze	0.6
Rime	1.0
Mixed	1.0

$\times 2.7\text{m}$  (height  $\times$  width) at the inlet. The height of the test section increases to 1.85m at the outlet to compensate for boundary layer growth. The background turbulence intensity for the tests Reynolds number is approximately 0.30%. The blocked area of the test section varied with AoA, however, the blockage was 5% in the worst case and thus no blockage correction was applied to the results. The experiments were conducted with chord based Re of  $4.55 \times 10^5$  ( $\pm 1.5\%$ ). This Re is slightly higher than that used by Krøgenes et al. [17]. However, they found only a small Re dependence between  $2 \times 10^5$  and  $4 \times 10^5$ , and thus the present results are believed to be directly comparable to their force measurements.

The airfoil used in the experiments is a NREL S826 airfoil [34], recommended for use on the blades of a horizontal axis wind turbines with a diameter of 20 – 40 m. The profile is designed to give high maximum lift coefficients, low profile-drag coefficients, and little sensitivity to leading edge roughness [34]. The airfoil was mounted vertically in the wind tunnel on a rotating force balance, which allowed for changes to the AoA with an accuracy of  $\pm 0.25^\circ$ .

The icing geometries used in this study, are the same as in Krøgenes et al. [17], and are described in detail in that work and by Hann [35]. They were found using LEWICE, and the physical icing was 3D-printed in PTA-plastic. All ice accretions were found for  $AoA = 1^\circ$ . For further information about LEWICE input conditions and the icing geometries, see Krøgenes et al. [17]. In total three icing cases were investigated: rime icing, glaze icing and mixed icing. Their geometries are shown in Fig. 2. Surface roughness of the ice accretions are shown in Table 1, with an accuracy of  $\pm 0.05$  mm. For comparison, the measurements were also performed on the clean airfoil. A total of seven AoA were investigated for all ice accretions and the clean case, namely  $-4^\circ$ ,  $0^\circ$ ,  $4^\circ$ ,  $6^\circ$ ,  $10^\circ$ ,  $14^\circ$  and  $16^\circ$ .

The mixed icing has a horn like geometry. The glaze and rime cases are more streamlined, but the rime accretion has a horn like feature protruding forward and appears as an extension of the chord. As identified in the introduction, there are multiple naming conventions for icing geometries. Here, the naming convention used in previous works from NTNU [17, 35] is used for ease of comparison. However, note that the physical geometry is more important than the name used to describe that geometry.

The PIV measurement plane was approximately 1.2m above the floor of the

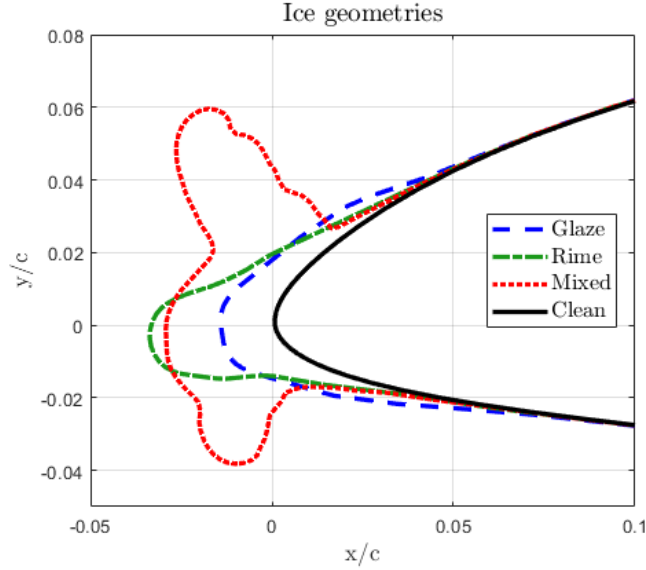


Figure 2: Ice geometries on the leading edge of the airfoil.

wind tunnel. The distance was far enough from the roof to ensure boundary layer effects were negligible. In addition, the distance from the box protecting the camera to the measurement plane was sufficiently large to ensure that the box had a negligible effect on the flow. Visual inspection with a smoke wand confirmed that the mean flow was approximately two dimensional in the measurement plane.

A Litron Nano L 200-15, ND-Yag double pulse laser, with a measured power of 208mJ, was used to illuminate the measurement plane. The laser was positioned underneath the wind tunnel, and redirected with mirrors before entering LaVision sheet optics. All optics were placed outside the wind tunnel, to ensure they did not disturb the flow. The laser sheet then entered the wind tunnel through one of the windows. Schematics of the setup are shown in Fig. 3a (front view) and Figure 3b (top view).

Seeding of the flow was done using a LeMaitre GForce 2 smoke machine. SAFEX Inside Nebelfluid Normal Power Mix and SAFEX Inside Nebelfluid Extra Clean fog fluids were used. Both are mixtures of diethylene glycol and water, and give particles with a diameter of approximately 1 micron.

## 2.2 Data acquisition

A pitot tube was used to measure the free stream velocity  $U_\infty$ . The atmospheric temperature  $T_{atm}$  was measured by a thermocouple in the wind tunnel. Both were measured at the start and end of each experimental run, and an average was used for the data acquired. Atmospheric pressure was found with a mercury

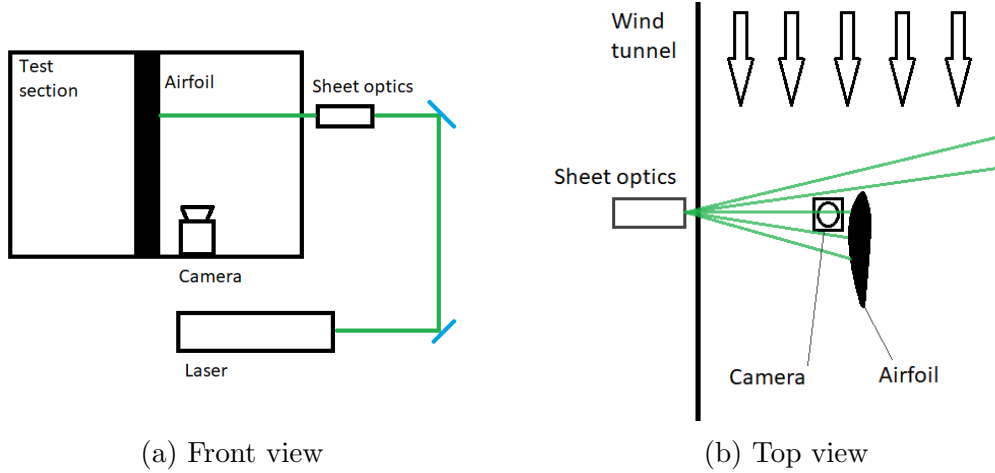


Figure 3: Schematics of the experimental setup.

barometer, at the start and the end of each day experiments were performed, and an average was calculated for that day.

To obtain the images, a LaVision Imager LX 16-megapixel camera was used. The bit depth of the camera is 12-bit. The lens used was a Sigma 105mm 1:2.8D DG Macro lens. The camera was mounted in an aerodynamically profiled box beside the airfoil, but still attached to the turntable. This ensured that the camera obtains the same field of view (FoV) for all icing geometries and AoA. The FoV was limited by the size of the airfoil and the power of the laser. With a larger FoV, the laser would not illuminate the measurement plane sufficiently for the experiments. The range of the FoV was  $-0.29 < x/c < 0.42$  and  $-0.03 < y/c < 0.45$ , where  $c$  is the chord length and the  $x$ -direction is parallel to the chord line. The data near the edges have been left out of the results, due to noise arising from particles entering or leaving the FoV.

A LaVision PTU X programmable timing unit (PTU) was used to synchronise and trigger the laser and the camera. It was controlled through LaVision DaVis (version 8.4) software. The time step between the two frames was set to  $80\mu\text{s}$ . All data were collected with a sampling frequency of 1.63Hz, ensuring that each vector field was statistically independent. For every AoA and for every icing geometry, 1000 samples were collected, which is sufficient to converge the first- and second-order turbulent statistics in this flow. This is shown for streamwise Reynolds stresses ( $\langle u^{*2} \rangle$ ) in Fig. 4, where the difference between the mean  $\langle u^{*2} \rangle$  calculated from the  $n$ -first samples and the final result for the same quantity, given as a percentage of the final  $\langle u^{*2} \rangle$ . It is calculated in a window of  $30 \times 29$  vectors, located in the shear layer, for mixed ice accretion at  $10^\circ$  AoA.

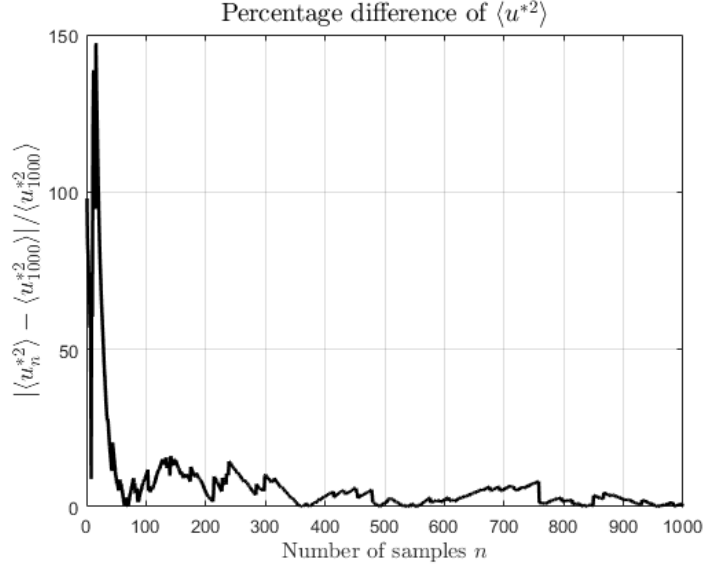


Figure 4: Difference between intermediate calculated and final streamwise Reynolds stresses  $\langle u^{*2} \rangle$ , given as a percentage of final  $\langle u^{*2} \rangle$ .

## 2.3 Processing

Processing of the data was done in LaVision DaVis (version 8.4). Preprocessing consisted of subtracting background noise from the images. First the minimum value of every pixel over the entire data set was subtracted, followed by subtracting the minimum over a filter length of 49. This two step process was used to both remove any ambient background signal as well as to account for time-varying changes in the lighting and seeding density. Processing was performed using GPU mode, with a window size of  $64 \times 64$  pixels and a window overlap of 50% for the first pass. The final window size was  $24 \times 24$  pixels, with a window overlap of 50%. Finally, bad vectors with too high correction value were deleted, and all empty spaces were filled with vectors calculated from the surrounding vectors. Parameters used in the data acquisition and processing are summarised in Table 2. All further processing and calculations has been made using MATLAB version R2017b.

The uncertainty of the mean velocity field was calculated in DaVis, and is normalised with the freestream velocity  $U_\infty$ . It is shown in Fig. 5 for mixed icing at  $AoA = 10^\circ$ . It was believed that this case would have amongst the highest uncertainties, as it is above stall  $AoA$  and has the most extensive ice geometry. The maximum value of the uncertainty is approximately 2.5% of  $U_\infty$ . Uncertainty has been evaluated for several other experimental cases, showing results with the same magnitude. The mean velocity field calculated in DaVis was subtracted from

Table 2: Summary of PIV parameters used in experiments and processing.

Parameter	Value	Unit
Frame separation	80	$\mu s$
Acquisition rate	1.63	Hz
Number of samples	1000	
Lens focal length	105	mm
Field of view ( $X \times Y$ )	$0.65 \times 0.42$	c (chord length)
Window size first pass	$64 \times 64$	Pixels
Final window size	$24 \times 24$	Pixels
Window overlap	50	%
Vectors ( $X \times Y$ )	$409 \times 276$	

the mean field calculated in MATLAB, and were found to be equal. This ensured that the uncertainty calculated was the same for both calculation methods.

### 3 Results

In this paper, the instantaneous velocity is referred to as  $\tilde{u}$ , for the x-direction, and is defined as  $\tilde{u} = U + u$ , where  $U$  is the mean quantity and  $u$  is the fluctuating part. The same applies for the perpendicular velocity component,  $\tilde{v}$ . The total velocities are denoted by subscript *tot*, such that  $\tilde{u}_{tot} = \sqrt{\tilde{u}^2 + \tilde{v}^2}$ .

For every experimental case, two different coordinate systems need to be used. One coordinate system is based on the chord of the airfoil. The x-axis is parallel to the chord line and the y-axis is perpendicular to the chord, with positive direction on the suction side of the airfoil. Therefore, this first coordinate system rotates with the airfoil and AoA. The second coordinate system remains fixed in the wind tunnel's frame, with the x-axis parallel to the mean flow and the y-axis perpendicular to it. All values given in the second coordinate system are denoted with a superscript \*, e.g  $u'^*$ , except the freestream velocity itself, which is denoted as  $U_\infty$ .

To ease visualisation, masks have been applied to the figures. A light grey mask covers the airfoil itself, a medium grey mask covers the ice accretion and a dark grey mask covers the laser shadow. The masks are applied after processing, and are not exact copies of the geometries. However, for the large FoV, the level of detail is limited, and the small extra region which might have been masked out is of limited interest.

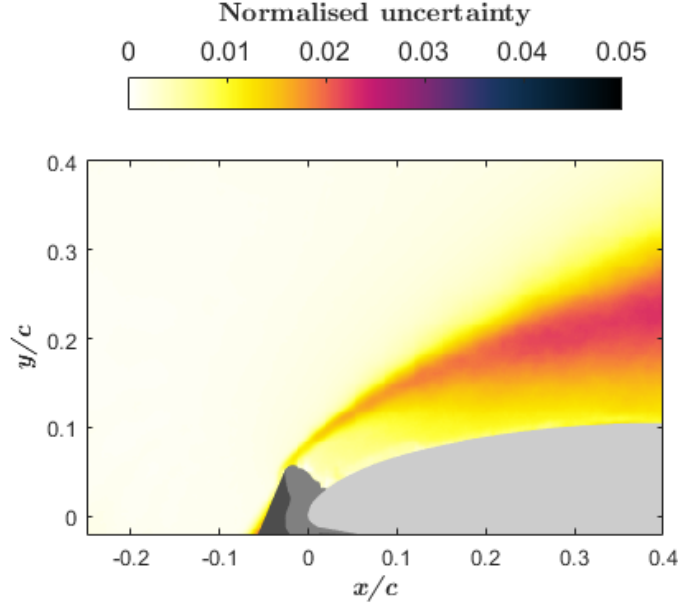


Figure 5: Uncertainty of the velocity for mixed ice accretion at  $AoA = 10^\circ$ , normalised by the freestream velocity.

### 3.1 Mean flow

The mean flow is normalised by  $U_\infty$ , and is shown in Fig. 6 for all icing cases and AoA.

In accordance with observations by Han et al. [4], the separation point is always located at the horn of the mixed ice accretion. The separation bubble increases in size for increasing AoA. When the AoA reaches  $6^\circ$ , it is not clear from the results if reattachment occurs for the mixed ice accretion. This is at the end of the linear lift region, and thus on the verge of stall. For all higher AoA, the increased size of the separation bubble indicates that the flow is unable to reattach, in accordance with the lift curve (Fig. 1). This is typical for thin airfoil stall, where a separation bubble separating at the leading edge is unable to reattach. The same type of stall was observed by Bragg et al. [10] for horn icing geometry.

This differs from the rime and glaze icing, and also the clean airfoil geometry. The shape of the  $C_l$  curves provided by Krogenes et al. [17] (Fig. 1) suggest that all investigated cases experience either trailing-edge stall or thin-airfoil stall, when compared to results obtained by Tani et al. [12]. As no separation bubble is visible in the results, it has been assumed that they are subjected to trailing edge stall, where separation starts near the trailing edge of the airfoil and moves

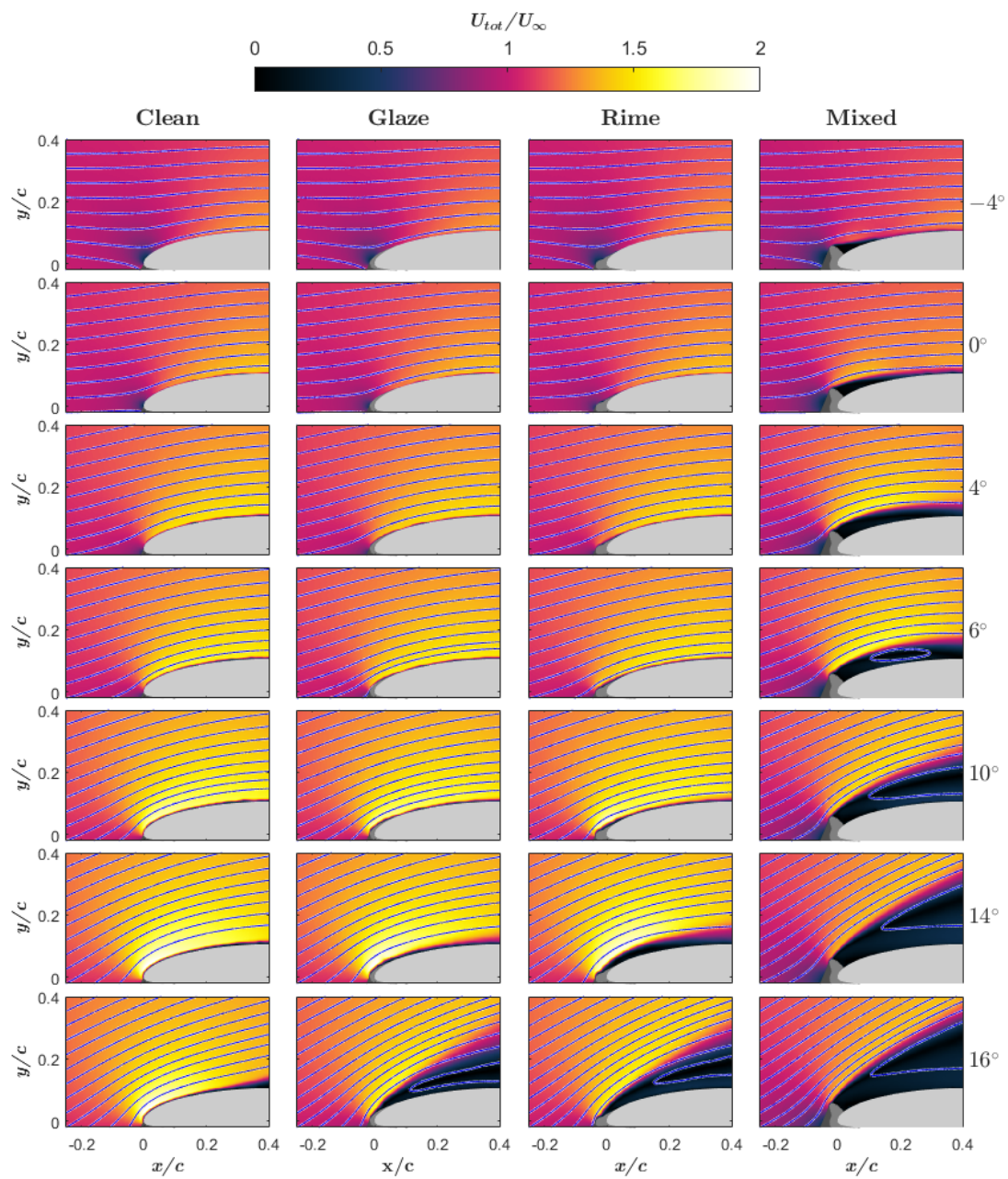


Figure 6: Mean velocities for all experimental cases normalised by the freestream velocity.



towards the leading edge with increasing AoA, until stall occurs [11].

When looking on the separation of the flow, the separation point is visible, but not at the leading edge, for the clean case at AoA  $16^\circ$ . The separation point is located at approximately  $x/c = 0.3$ . This also suggest that the separation point is moving from the trailing edge to the leading edge, and that trailing-edge stall occurs for the clean airfoil. It is apparent that the rime and glaze geometries lead to separation closer to the leading edge. For the rime ice accretion, this is visible also at  $AoA = 14^\circ$ . The reason for this is probably the increased turbulence resulting from the roughness of the ice [9]. This will be demonstrated and discussed further in the next section.

One interesting feature of the  $C_l$  curve in Fig. 1 for the glaze accretion, is the increase in  $C_l$  from AoA  $12^\circ$  to  $13^\circ$  and  $14^\circ$ . At AoA  $14^\circ$ , the low speed region over the airfoil grows, so stall was expected at this AoA. However, this low speed layer is likely of insufficient thickness to cause stall, and the flow might thus stay attached over the entire airfoil. Furthermore, for rime accretion,  $C_l$  is generally smaller than for the clean case, but not for AoA ranging from  $12^\circ$  to  $14^\circ$ . In this region, it is as large as the curve for the clean airfoil. One reason for these phenomena might be that the icings act as a leading edge slat. Such behaviour has been reported in earlier works, for streamwise ice accretions at high AoA [4, 19, 20]. Further investigation was undertaken to uncover if the high  $C_l$  was due to this phenomena.

If the ice accretion acted as a leading edge slat, an increase in the effective AoA would be expected. The angle of the incoming flow was computed as an average of the flow at  $x/c = -0.2$  in the FoV. The results are shown in Fig. 7. Looking at  $AoA = 14^\circ$ , the effective AoA does not increase for the glaze accretion compared to the effective AoA for the clean case. The bump in the  $C_l$  curve is therefore not believed to come from the icing acting as a slat. The rime accretion does lead to a small increase of the effective AoA, which makes it possible that the large  $C_l$  values in this region occurs because the accretion acts as a leading edge slat.

The relation between  $C_l$  and the difference of effective AoA and actual AoA is shown in Fig. 8. For all ice accretions and the clean airfoil, stall happens when the difference is between  $12^\circ$  and  $14^\circ$ . The rime icing experiences maximum lift at a higher effective AoA than the others, while mixed icing experience maximum lift at a lower effective AoA. Thus, streamlined ice accretions allows reattachment at higher effective AoA than the clean airfoil, which indicates that the icing possibly could act as a slat. However, this is not conclusive, as the separation happening at high AoA might be the reason for the increased effective AoA.

The drag increases with increasing size of the separation bubble for mixed ice accretion. The separation bubble leads to high drag also for low and negative

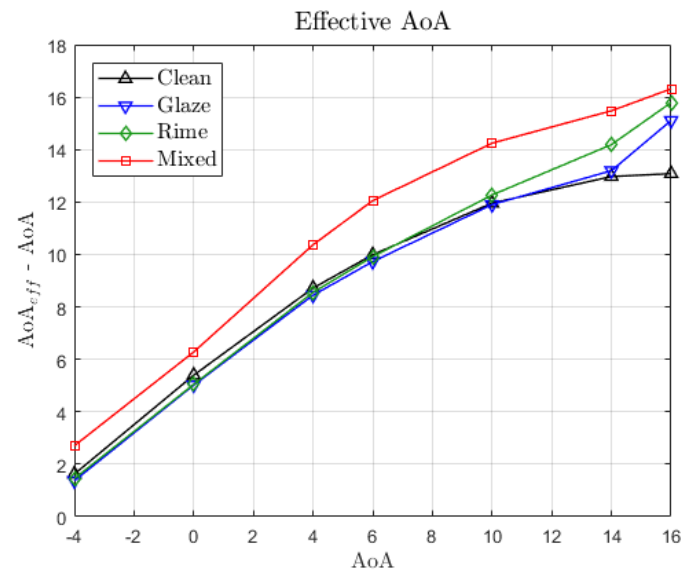


Figure 7: Difference between effective AoA and actual AoA, measured at  $x/c = -0.2$ .

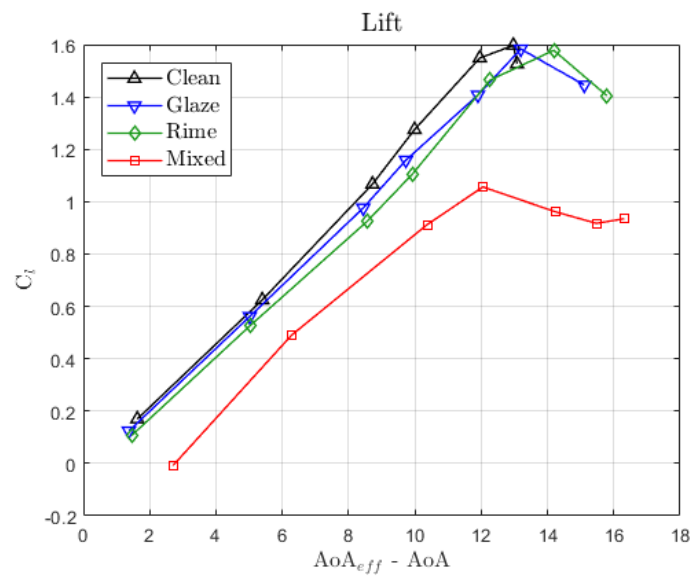


Figure 8: Lift coefficient  $C_l$  as function of the difference between effective AoA at  $x/c = -0.2$  and actual AoA.

AoA. For the other ice accretions, the increase in drag is largest compared to the clean airfoil when separation is visible in the FoV. Thus, separation is the most important factor for the increase in drag. However, the roughness of the icing also leads to increased skin friction drag.

As the drag is low for glaze icing at  $AoA = 14^\circ$ , it is believed that flow stays attached over the airfoil. This, combined with the lack of increase in effective AoA compared to the clean case, suggests that some mechanism in the flow, occurring due to the icing, keeps the flow attached farther downstream on the airfoil surface than what would be expected. It is unfortunately not possible to describe the flow physics farther downstream above the airfoil from the data obtained.

### 3.2 Turbulent kinetic energy

The turbulent kinetic energy (TKE),  $k$ , was calculated as

$$k_{2D,normalised} = \frac{1}{2} \frac{\langle u^2 \rangle + \langle v^2 \rangle}{U_\infty^2}, \quad (1)$$

and is a two dimensional surrogate.  $U_\infty^2$  was used to normalise the value.

Fig. 9 shows TKE of the different experimental cases. The figure suggests that most of the TKE is associated with flow separation. For the mixed accretion, the turbulence is found in the shear layer between the reverse flow inside the separation bubble and the freestream flow. The turbulent shear layer is thin close to the ice horn, and grows wider until it reaches the reattachment point. The wide region of turbulence close to the airfoil indicates that the reattachment point is fluctuating. The fluctuations and the shape of the shear layer are in accordance with several earlier publications on the separation bubble downstream of horn icing [21, 22].

The shear layer is at its widest when AoA is  $10^\circ$  for mixed icing. This indicates that the flow is highly unstable in the wake of the ice horn. From the figure, it seems like the flow reattaches at some instances, as the shear layer hits the airfoil. It is stalled at higher AoA, with the turbulent kinetic energy moving far from the airfoil surface. Instantaneous velocity fields have been produced to investigate this phenomena further. Four samples are presented for each of the three highest AoA for mixed ice accretion in Fig. 10.

For  $10^\circ$  AoA, the extension of separated flow is varying from less than  $y/c = 0.2$  to about  $y/c = 0.36$  at the edge of the FoV. This variation is higher than for both  $14^\circ$  and  $16^\circ$  AoA. For  $14^\circ$  the extension is close to  $y/c = 0.30$  for all instantaneous measurements presented. The corresponding value for  $16^\circ$  is  $y/c = 0.33$ . This complies with the assumption that the wide region of high TKE in the mean flow is due to more variation in the flow field. Note that only four

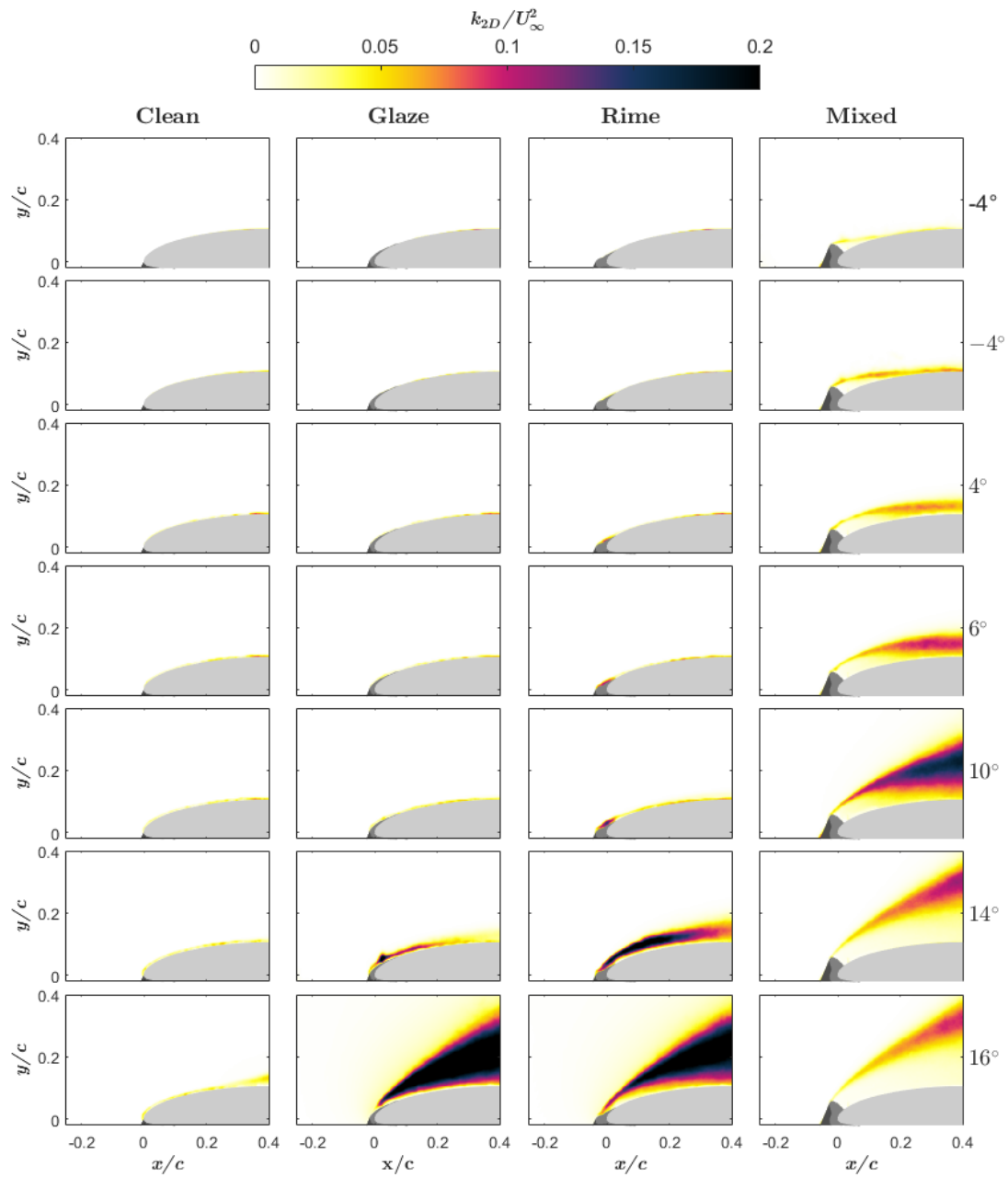


Figure 9: Two dimensional turbulent kinetic energy surrogate for all experimental cases, normalised by the freestream velocity.

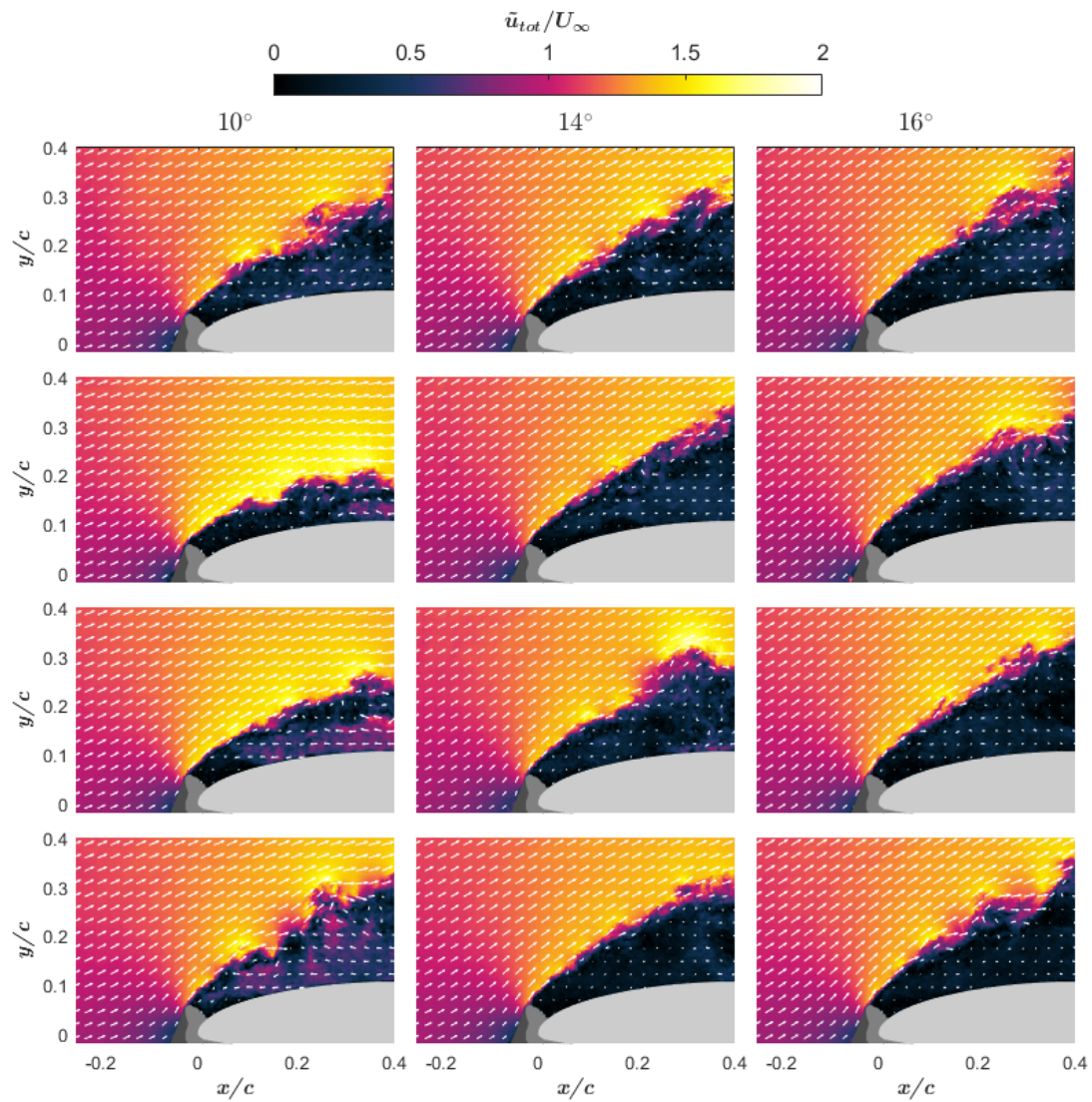


Figure 10: Instantaneous velocities for mixed ice accretion at  $AoA = 10^\circ, 14^\circ$  and  $16^\circ$ .

measurements have been evaluated for each case, so other instantaneous images could possibly show other results.

Both for the rime and glaze icing cases, the energy is high for  $AoA = 16^\circ$ , which is above the stall angle. The turbulent region starts at the leading edge, in contrast to the clean case, where the turbulent region starts farther downstream. This is in agreement with the mean flow, as the separation happens farther downstream without ice accretion. At  $AoA = 14^\circ$ , the rime accretion also leads to turbulent flow over the entire airfoil. For the glaze accretion the turbulence generated seems to decay downstream of the icing. This indicates that the flow is still attached for this angle, and might stay attached downstream of the FoV as well. It agrees with what is observed in the mean results. The spot where the TKE footprint is wider than the rest of the TKE layer is believed to be noise associated with laser sheet reflection from the airfoil surface.

Focusing on the rime accretion on lower AoA ( $4^\circ - 10^\circ$ ), some TKE is observed above the ice geometry. This is an indication that the roughness of the ice leads to turbulent transition of the boundary layer at the leading edge. Bragg et al. [9] states that the roughness usually is higher than the local boundary layer, which leads to turbulent transition. This is also the reason why the separation point moves forward on the airfoil for the streamwise ice accretions. The effect of the roughness is higher for rime ice, as the height of the roughness is larger, but the slightly more extensive geometry also contributes to the transition.

For all cases without stall and recirculation, some TKE is observed close to the airfoil. It is not known if this is noise from reflections or actual measurements at this state. The fact that it is not present underneath the recirculating regions for high AoA, might indicate that they represent energy in the flow, and that turbulent transition of the boundary layer has happened for these cases. However, the uncertainty is large for these observations, and no conclusions are drawn.

### 3.3 Vorticity

The two dimensional instantaneous vorticity  $\Omega$  of the flow has been calculated and normalised according to

$$\Omega_{normalised} = \left( \frac{d\tilde{v}}{dx} - \frac{d\tilde{u}}{dy} \right) \cdot \frac{c}{U_\infty}, \quad (2)$$

which gives clockwise vorticity for negative values and counter-clockwise for positive values.

The mean of the vorticity for all experimental cases have been calculated, and the results are presented in Fig. 11. In all cases, a checker pattern can be seen in the flow outside the high vorticity regions. The Moiré fringes are not physical, but errors occurring due to having a large field of view in the data acquisition.

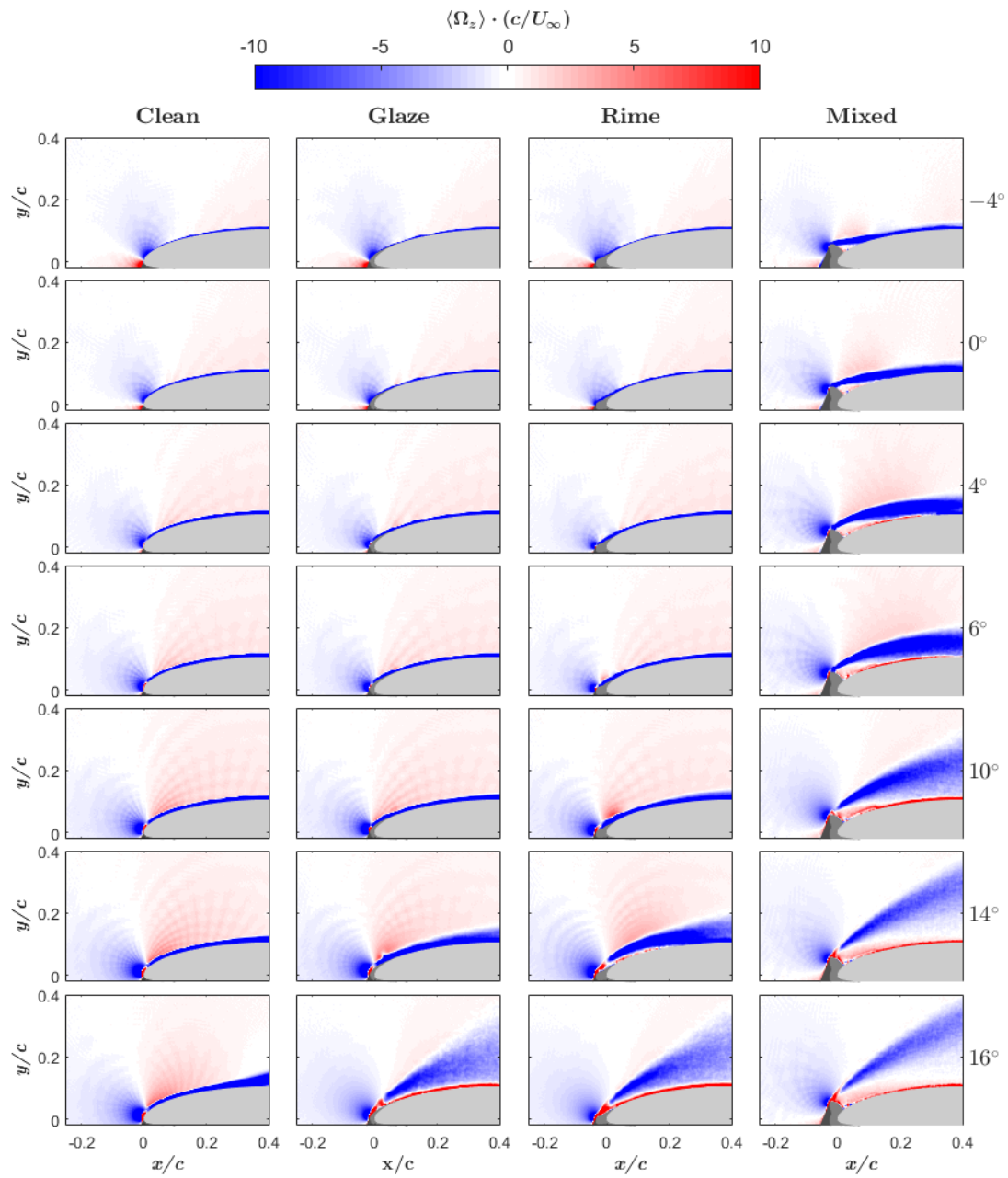


Figure 11: Normalised mean vorticity for all experimental cases.

The vorticity is clockwise near the suction side of the airfoil for all regions where recirculation does not occur. This is due to the boundary layer, where the velocity increases with increased distance from the airfoil. When the flow has separated, the flow close to the airfoil surface is opposite in direction, and the boundary layer gives counter-clockwise vorticity. For the mixed icing case clockwise vorticity is also observed for a small region just downstream of the horn, close to the airfoil surface. The region is small, and may be noise rather than actual measurements. However, the observation is in agreement with the structure of the bubble, as reported earlier by Jacobs and Bragg [21, 27].

For rime ice accretion, at  $AoA = 14^\circ$ , counter clockwise vorticity is observed close to the airfoil surface. This indicates a thin recirculating region, which is not evident in the mean velocity field (Fig. 6) or the TKE field (Fig. 9). The streamwise horn acts more like a regular horn geometry at high AoA, as the flow separates at the leading edge. The separation bubble increases the drag of the airfoil, compared to the clean case, more than what roughness effects seem to do for lower AoA. The lift of the airfoil is not reduced by the phenomena. In fact, this is the only region where the  $C_l$  (Fig. 1) for any of the ice accretions is as large as for the for the clean case.

For the experimental cases where the flow separates, the vorticity is high in and around the shear layer described earlier. This is the same region as where the turbulent energy is highest. The mean vorticity is clockwise in this regions, showing that the main vortices coming from the separation point rotate clockwise. This is in agreement with the instantaneous velocity fields in Fig. 10 where clockwise vortices were observed. The layer of clockwise mean vorticity is larger for  $AoA = 10^\circ$  than higher AoA, when looking on mixed ice accretion. This indicates that the layer of high vorticity is varying in the instantaneous fields. This complies with what is observed for the TKE in Fig. 9 and the unstable flow observed in Fig. 10.

The mean vorticity is not significantly affected by the streamwise icing geometries, rime and glaze, for the lower AoA. The region of negative vorticity is thicker than what is observed for the clean case only for  $AoA = 14^\circ$  for glaze ice accretion and for  $10^\circ$  and  $14^\circ$  for rime ice accretion. The vorticity around the leading edge is positive. It is at present not known if this is due to reflections from the airfoil, which rotates towards the laser sheet, or due to the boundary layer being sufficiently thin. If the latter is the case, the decreased velocity close to the airfoil surface is not captured by any vectors. Thus, the velocity measured close to the airfoil would be higher than the velocity farther away, and the vorticity would be positive.



The swirl strength  $\lambda_s$  was found according to

$$\lambda_s = \max \left[ 0, -\frac{1}{2} \left( \frac{d\tilde{u}}{dy} \cdot \frac{d\tilde{v}}{dx} - \frac{d\tilde{u}}{dx} \cdot \frac{d\tilde{v}}{dy} \right) + \frac{1}{4} \left( \left( \frac{d\tilde{u}}{dx} \right)^2 + \left( \frac{d\tilde{v}}{dy} \right)^2 \right) \right], \quad (3)$$

and was normalised with  $(c/U_\infty)^2$ . To take the direction of the swirl into account, it was also multiplied by the sign of the instantaneous vorticity, calculated as in equation 2. That means the positive swirl is counter-clockwise, in the same way as the positive vorticity.

The instantaneous swirl strength is shown in Fig. 12, for all experimental cases. Many of the same observations made for the mean vorticity apply for the swirl. Near the leading edge, the swirl strength increase with increasing AoA. From AoA of  $10^\circ$  and  $6^\circ$ , the effect of icing are visible for glaze and rime accretions respectively, with a thicker layer of increased swirl strength.

Generally, when the flow is attached, the swirl is clockwise close to the airfoil. When recirculation occurs, the swirl changes direction, and becomes counter-clockwise close to the airfoil. As for vorticity, counter-clockwise swirl is observed close to the airfoil for rime ice accretion at  $14^\circ$  AoA. This substantiates the existence of a separation bubble for this particular case.

In the shear layer of the different flows, the swirl is mostly negative. Outside the shear layer, the accelerated flow leads to positive swirl, due to the deflections of the streamlines.

The region close to the airfoil leading edge does not show any positive swirl, as was the case for the mean vorticity. This indicates that there is noise in the measurements, leading to the observation of the positive vorticity. This might be due to reflections from the surface of the airfoil or icing, which changes when the AoA is changed. Therefore, no conclusions are drawn from the vorticity close to the leading edge of the airfoil.

## 4 POD analysis

### 4.1 POD analysis

Snapshot POD, developed by Sirovich [36], was used to find the spatial modes of the flow. The computations were performed in the same manner as by e.g Meyer et al. [37, 38], and the methodology is described below.

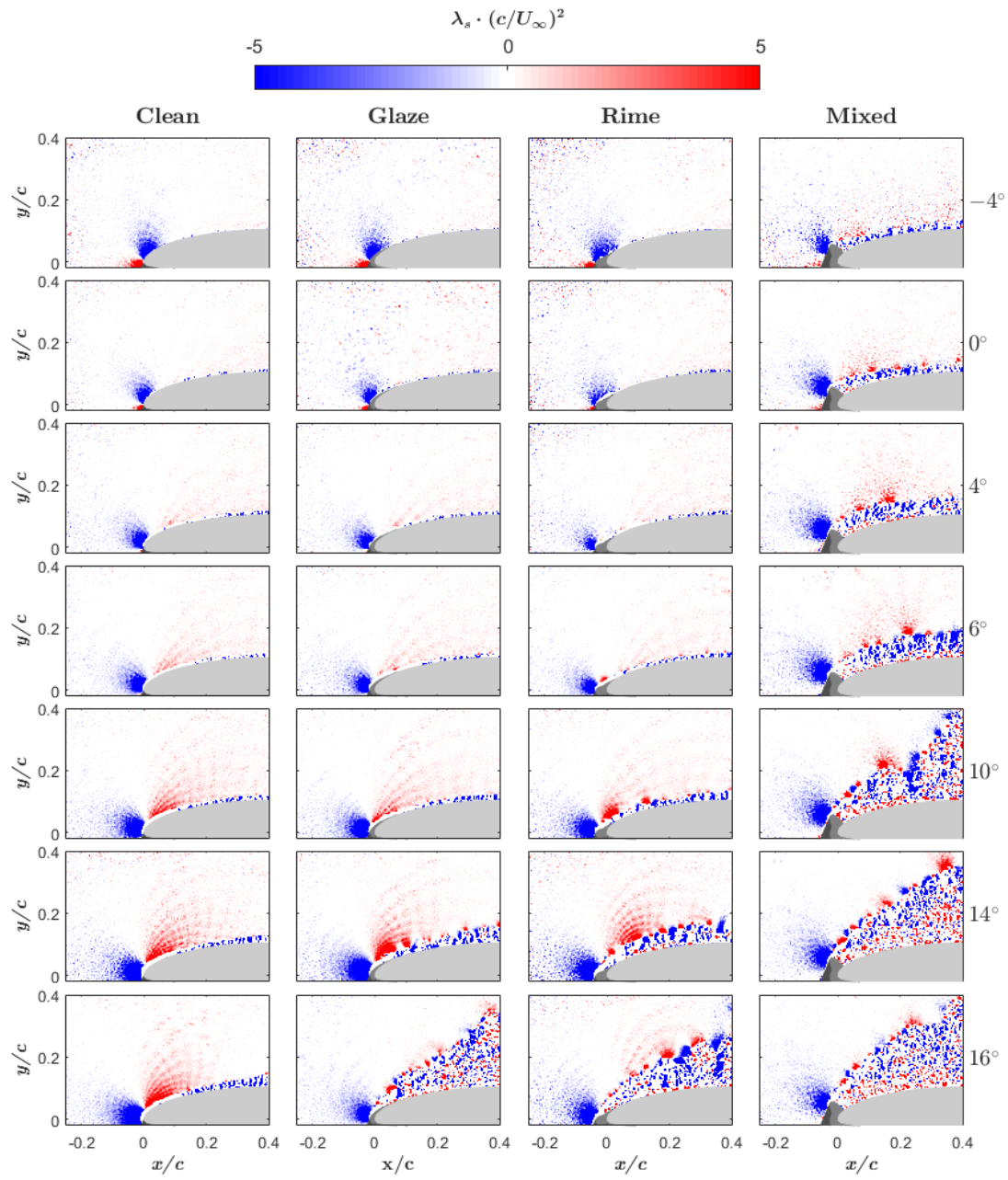


Figure 12: Normalised instantaneous swirl strength for all experimental cases.

All the fluctuating velocity components are stored in a matrix,

$$\mathbf{U} = [\mathbf{u}^1 \quad \mathbf{u}^2 \quad \cdots \quad \mathbf{u}^N] = \begin{bmatrix} u_1^1 & u_1^2 & \cdots & u_1^N \\ \vdots & \vdots & \ddots & \vdots \\ u_M^1 & u_M^2 & \cdots & u_M^N \\ v_1^1 & v_1^2 & \cdots & v_1^N \\ \vdots & \vdots & \ddots & \vdots \\ v_M^1 & v_M^2 & \cdots & v_M^N \end{bmatrix}, \quad (4)$$

where each column is for one of the snapshots, or instantaneous velocity fields. The order of the velocity components must be the same in every column.  $N$  is the number of snapshots, or data sets, and  $M$  is the total number of velocity vectors in the data.

The next step is to create the autocovariance vector

$$\tilde{\mathbf{C}} = \mathbf{U}^T \mathbf{U}, \quad (5)$$

and solve the corresponding eigenvalue problem

$$\tilde{\mathbf{C}} \mathbf{A}^i = \lambda^i \mathbf{A}^i. \quad (6)$$

The eigenvalues in  $\boldsymbol{\lambda}$  are sorted from high to low, and represent the energy of each mode. The corresponding eigenvectors  $\mathbf{A}^i$  are then used to construct the POD modes

$$\boldsymbol{\Phi}^i = \frac{\sum_{n=1}^N \mathbf{A}_n^i \mathbf{u}^n}{\left\| \sum_{n=1}^N \mathbf{A}_n^i \mathbf{u}^n \right\|}, i = 1, \dots, N., \quad (7)$$

where  $A_n^i$  corresponds to  $\lambda^i$ . Now, the new velocity vectors can be extracted from the modes in the same order as in the matrix  $\mathbf{U}$ .

To reconstruct the flow field, the POD coefficients

$$a_i = \boldsymbol{\phi}^i \mathbf{u}^n \quad (8)$$

are calculated. The fluctuating snapshots can now be reconstructed according to

$$\mathbf{u}^n = \sum_{i=1}^N a_i^n \boldsymbol{\phi}^i, \quad (9)$$

and the mean flow and other quantities can be calculated from the new snapshots.

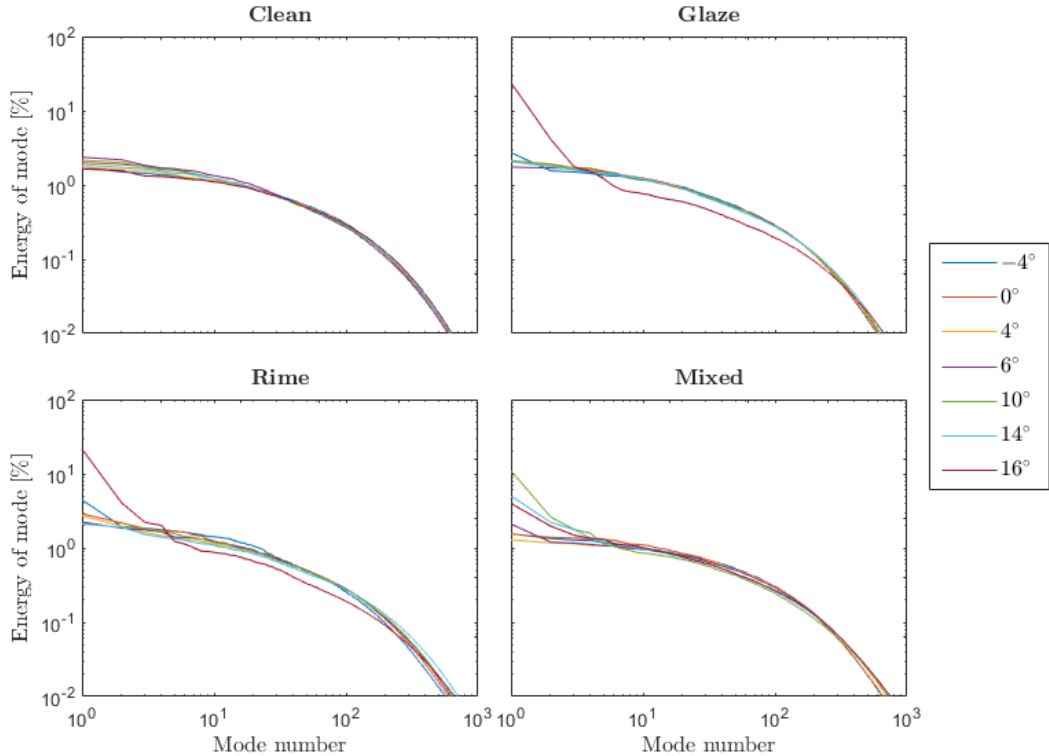


Figure 13: Energy of the modes calculated for all experimental cases, given as the percentage of total energy for the case.

## 4.2 Energy of modes

It is interesting to see whether any of the modes capture much of the energy in the flow, as this indicates the existence of coherent structures in the flow. Fig. 13 displays plots of the energy of the modes for the fluctuating velocity components at all AoA and icing geometries. The first observation is that for all cases where the flow is attached through the field of view, no high energy modes are observed. Therefore, no high energy modes are found for the clean case.

For the glaze and rime cases, high energy modes are found for  $AoA = 16^\circ$ , and also to some extent for  $AoA = 14^\circ$ . This indicate that coherent structures are found in these flow fields. The energy curves for  $AoA = 16^\circ$  for both mentioned accretions look similar, which indicate that the flow fields look similar. A further comparison between the accretions at  $AoA = 16^\circ$  has been made, and will be discussed in the next section.

When looking on the mixed icing case, the most energetic modes are found

at  $AoA = 10^\circ$ , but also for  $6^\circ$ ,  $14^\circ$  and  $16^\circ$  high energy modes are found. The energy is decreasing with  $AoA$  higher than  $10^\circ$ . This indicates that there are more coherent structures when  $AoA = 10^\circ$ , than for higher  $AoA$ . Fig. 9 shows that TKE is high for a larger vertical distance in this case, indicating larger structures in the flow. Together these observations lead to a conclusion that the coherent structures are more important for the flow field for this case, compared to higher  $AoA$ .

### 4.3 POD modes for $AoA = 16^\circ$

The first five POD modes for the fluctuating velocity components  $16^\circ$   $AoA$ , for all icing cases, are shown in Fig. 14 ( $x^*$ -component) and Fig. 15 ( $y^*$ -component). Only small fluctuations close to the airfoil are present for the case without ice accretion. As the separation happens farther behind on the airfoil surface, at approximately  $x/c = 0.3$ , the separated region where most of the turbulence exists, is not captured in the FoV.

For glaze and rime ice accretions, the first four modes show similar behaviour, both for the  $x^*$ -component and the  $y^*$ -component. Note that the sign of the component does not matter when comparing modes, since all modes are made from bases being orthogonal to each other. The fifth mode shows different behaviour for the two cases. This means that the first four modes, containing 31% and 30% of the flow fluctuating energy for glaze and rime ice accretions respectively, will give a similar reconstruction of the flow. About 30% of the energy of the flows are then from the same structures.

### 4.4 Reconstruction of flow

For rime ice accretion,  $AoA = 16^\circ$ , the flow field has been reconstructed from the 15 most energetic modes. In total, they account for 39.9% of the fluctuating energy of the flow. The reconstructed  $x$ -component of the velocity has been compared to the measured  $U$ , and the two flow fields are shown in Fig. 16. The main features of the flow is captured in the reconstruction, including the approximate size of the recirculating region of the flow. This means that the main features of the flow are contained in a small number of modes, indicating that if an active control methodology was sought to combat the effects of icing, reduced order modelling could be used to focus on only a few modes, thus improving feedback time and flow estimates.

A quantitative measurement of the quality of the reconstruction is provided through the absolute error of the reconstruction, and is displayed in Fig. 17. All absolute values of the normalised error are well below 0.2, or 20% of the freestream velocity. However, the error is highest in the separated region and the

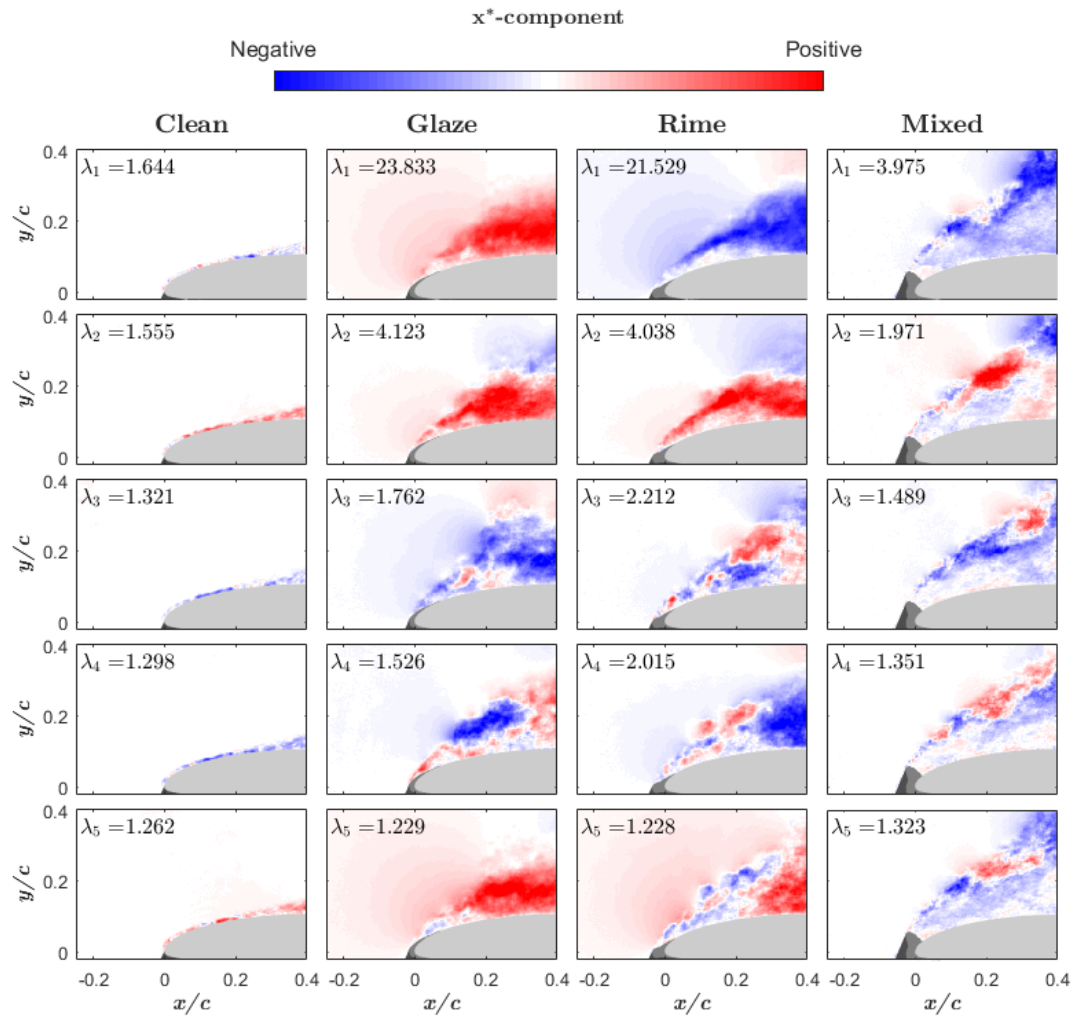


Figure 14: Five first  $x^*$ -direction velocity modes for  $AoA = 16^\circ$ , for all ice accretions and the clean airfoil.

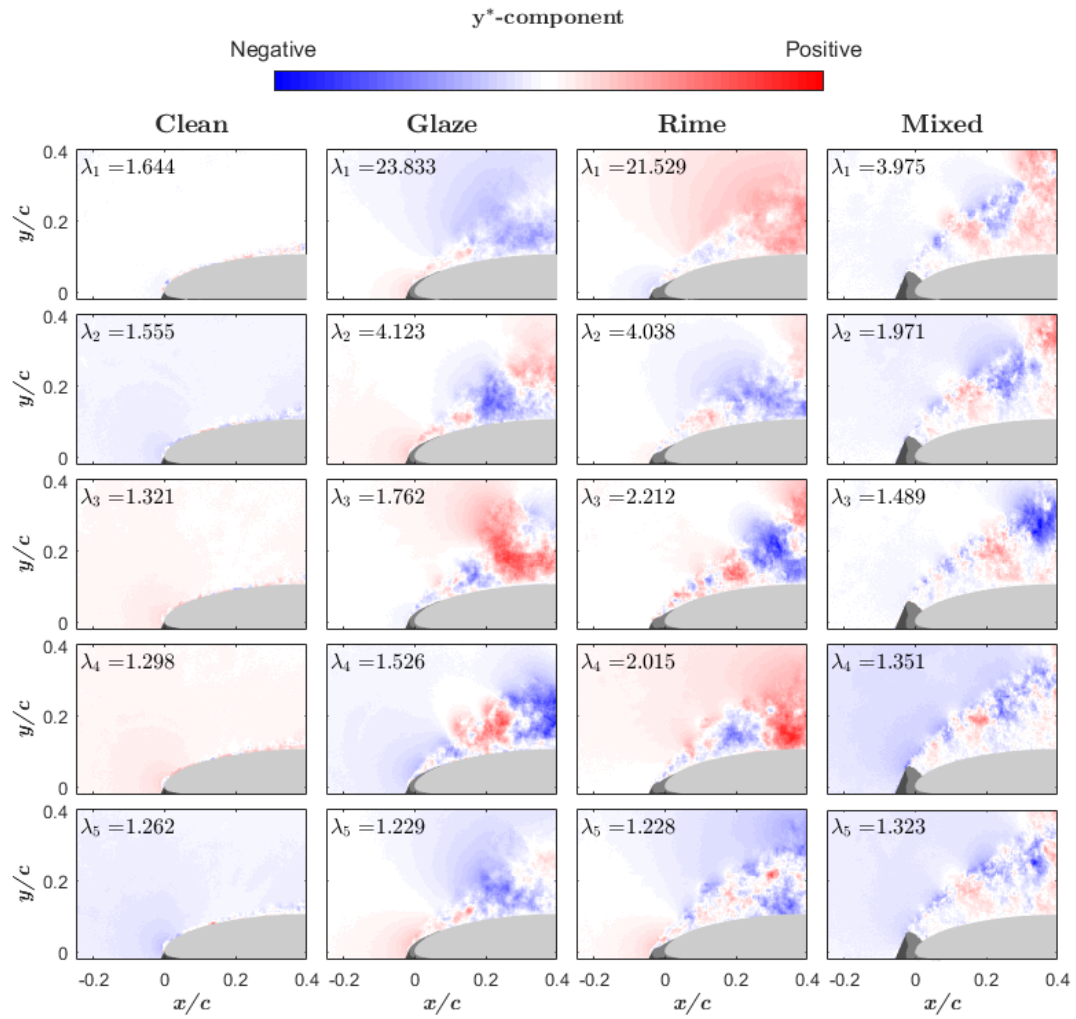


Figure 15: Five first  $y^*$ -direction velocity modes for  $AoA = 16^\circ$ , for all ice accretions and the clean airfoil.

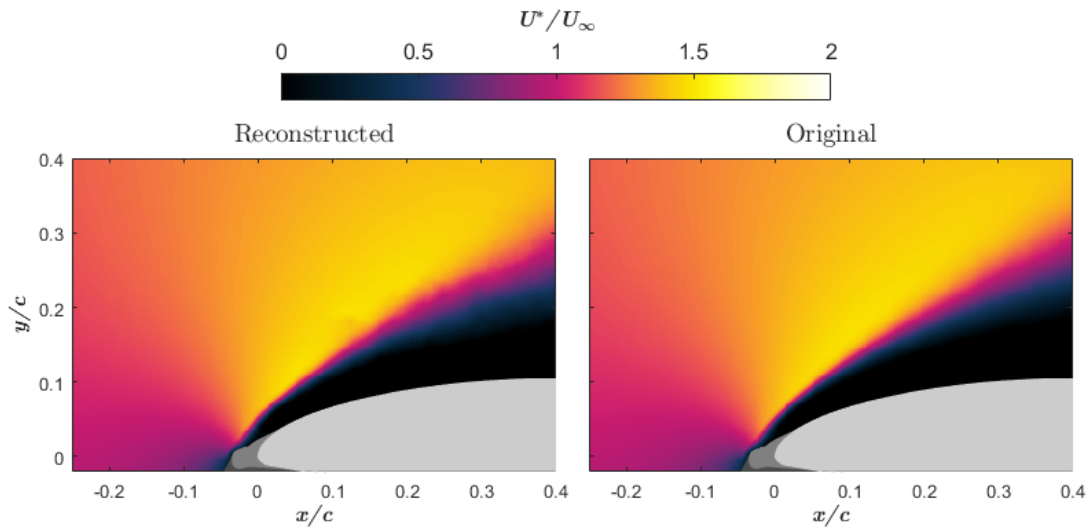


Figure 16: Comparison of the mean flow field reconstructed from the first 15 POD modes and the mean flow field obtained experimentally, for rime ice accretion at  $AoA = 16^\circ$ .

shear layer. Especially in the recirculating region, the velocities are small, so the relative error in this region is large. Despite the high relative error, the error is small in magnitude, which leads to the assumption that the reconstruction is of a quality that makes POD useful for this flow.

To see if the same reconstruction is possible for the other cases, the number of modes needed to reconstruct 40% of the flow field for the experimental cases is shown in Fig. 18. For glaze and rime accretions at  $AoA = 16^\circ$  approximately 15 modes is enough, in contrast to all other experimental cases. The sharp drop in the number of modes indicate that the separated flow for these cases are dominated by coherent structures, while there are no such structures at lower  $AoA$ . It is also interesting that the mixed case needs a high number of modes to be reconstructed. This leads to a conclusion that the flow inside the recirculation bubble is not dominated by any coherent structures when it reattaches to the airfoil. There is also a sharp drop in the number of modes needed to reconstruct the flow over the mixed icing at  $AoA = 10$ , which indicates that there are coherent structures for this case, even though a high number of modes are needed for reconstruction. At higher  $AoA$ , a larger number of modes are needed to reconstruct the flow, indicating fewer coherent structures. These observations are in agreement with the earlier discussed energy content of the modes.



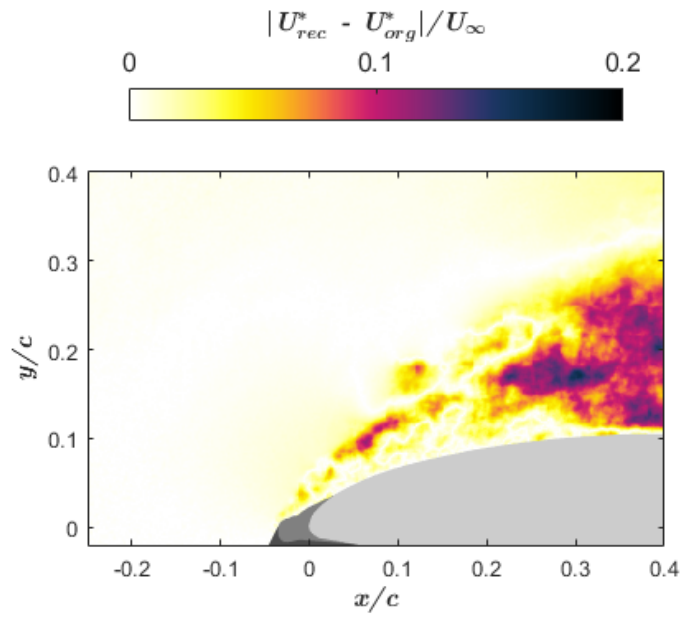


Figure 17: Absolute value of error in the flow field reconstructed from 15 modes, for rime ice accretion at  $AoA = 16^\circ$ .

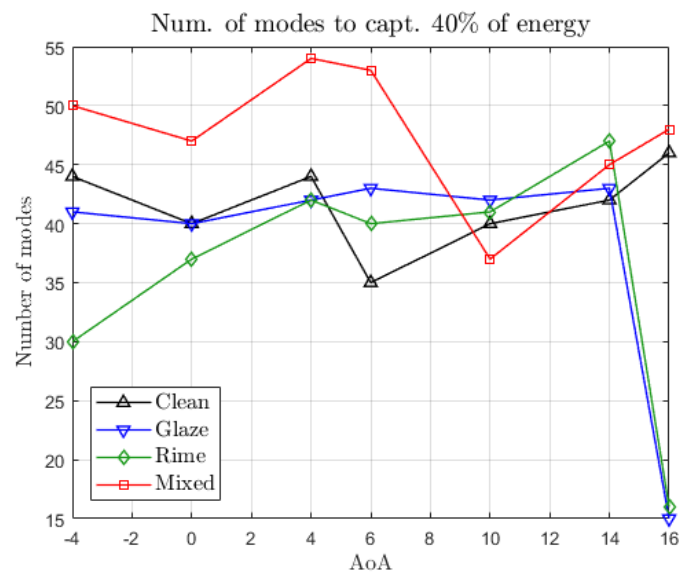


Figure 18: Number of modes needed to capture 40% of the energy of the fluctuations in the flow.

## 5 Conclusion

PIV measurements have been performed on an NREL S826 airfoil subjected to icing. Three different ice accretion geometries have been used, and the clean case was also investigated as a reference. Experiments have been performed on angles of attack ranging from  $-4^\circ$  to  $16^\circ$ .

Mean velocity fields show a separation bubble behind the horn of the mixed ice accretion, which grows in size with increasing AoA. Turbulent kinetic energy is high in the shear layer separating the recirculating region from the inviscid flow. For  $AoA = 10^\circ$ , the shear layer is unstable, and it seems like the flow is close to reattachment at some instantaneous measurements, while the recirculating region is wide at other moments.

For the streamlined ice accretions (glaze and rime), separation is visible in the field of view from angle of attack above  $14^\circ$  in the mean flow field, and happens close to or at the leading edge. This means separation happens farther upstream on the airfoil than for the clean case. Turbulent kinetic energy is high in the entire recirculating region and the shear layer when the flow is separated. Recirculation, and thus separation, is found for rime accretion at  $AoA = 14^\circ$ , but it seems like the flow is able to reattach most of the time. This is in accordance with the lift curve, which states that this is on the verge of stall conditions. At the same angle of attack, glaze accretion does not lead to a permanent separation bubble, but the high level of turbulent kinetic energy might indicate that the flow is separating at some time instances. This also confirms that the flow is on the verge of stalling.

POD has shown that high energy modes are present for experimental cases where the flow has separated. For the same cases, reconstruction of the main properties of the flow field is possible from a limited number of modes. The flow inside the recirculating region is not accurately reconstructed, but the height of the shear layer is correct in the reconstruction. This means that control of the flow is possible using only a limited number of modes.

## References

1. Renewables 2017 Global Status Report. *Paris: REN21 Secretariat* (2017).
2. Parent, O. & Ilinca, A. Anti-icing and de-icing techniques for wind turbines: Critical review. *Cold Regions Science and Technology* **65**, 88–96 (1 2011).
3. Botta, G., Cavaliere, M. & Holttinen, H. *Ice accretion at Acqua Spruzza and its effects on wind turbine operation and loss of energy production in Proceedings of BOREAS IV* (Apr. 1998).
4. Han, Y., Palacios, J. & Schmitz, S. Scaled ice accretion experiments on a rotating wind turbine blade. *Journal of Wind Engineering and Industrial Aerodynamics* **109**, 55–67 (2012).
5. *Aircraft Icing Handbook* (Civil Aviation Authority of New Zealand, 2000).
6. Homola, M. C., Wallenius, T., Makkonen, L., Nicklasson, P. J. & Sundsbø, P. A. The relationship between chord length and rime icing on wind turbines. *Wind Energy* **13**, 627–632 (2009).
7. Etemaddar, M., Hansen, M. O. L. & Moan, T. Wind turbine aerodynamic response under atmospheric icing conditions. *Wind Energy* **17**, 241–265 (2 2014).
8. Han, Y. & Palacios, J. Airfoil-performance-degradation prediction based on nondimensional icing parameters. *AIAA Journal* **51**, 2570–2581 (2013).
9. Bragg, M. B. *et al.* Airfoil ice-accretion aerodynamics simulation in *Proceedings of 45th AIAA Aerospace Meeting & Exhibition conference* (AIAA, Jan. 2007).
10. Bragg, M. B., Broeren, A. P. & Blumenthal, L. A. Iced-airfoil aerodynamics. *Progress in Aerospace Sciences* **41**, 323–362 (5 2005).
11. McCullough, G. B. & Gault, D. E. Examples of three representative types of airfoil-section stall at low speed. *NACA Technical Note 2502* (1951).
12. Tani, I. Low speed flows involving bubble separation. *Progress in Aerospace Sciences* **5**, 70–103 (1964).
13. Hochart, C., Fortin, G., Perron, J. & Ilinca, A. Wind turbine performance under icing conditions. *Wind Energy* **11**, 319–333 (4 2008).
14. Barber, S., Wang, Y., Jafari, S., Chokani, N. & Abhari, R. S. The Impact of Ice Formation on Wind Turbine Performance and Aerodynamics. *Journal of Solar Engineering* **133** (2011).
15. Virk, M. S., Homola, M. C. & Nicklasson, P. J. Effect of rime ice accretion on aerodynamic characteristics of wind turbine blade profiles. *Wind Engineering* **34**, 207–218 (2 2010).

16. DeGregorio, F., Ragni, A., Airoidi, M. & Romano, G. P. *PIV investigation on airfoil with ice accretions and resulting performance degradation in Proceedings of ICIASF 2001 Record, 19th International Congress on Instrumentation in Aerospace Simulation Facilities (Cat. No.01CH37215)* (Aug. 2001), 94–105.
17. Krøgenes, J. *et al.* Aerodynamic performance of the NREL S826 airfoil in icing conditions. *Master thesis, NTNU* (2017).
18. Pouryoussefi, S. G., Mirzaei, M., Nazemi, M.-M., Fouladi, M. & Doostmahmoudi, A. Experimental study of ice accretion effects on aerodynamic performance of an NACA 23012 airfoil. *Chinese Journal of Aeronautics* **29**, 585–595. ISSN: 1000-9361 (2016).
19. Jasinski, W. J., Noe, S. C., Selig, M. S. & Bragg, M. B. Wind turbine performance under icing conditions. *Journal of Solar Energy Engineering* **120**, 60–65 (1 1998).
20. Gray, V. H. & von Glahn, U. H. Aerodynamic effects caused by icing of an unswept NACA 65A004 airfoil. *National Advisory Committee for Aeronautics*.
21. Jacobs, J. J. & Bragg, M. B. *Particle image velocimetry measurements of the separation bubble on an iced airfoil in Proceedings of 24th AIAA Applied Aerodynamics Conference* (American Institute of Aeronautics and Astronautics, June 2006).
22. Jacobs, J. J. & Bragg, M. B. *Two- and three-dimensional iced airfoil separation bubble measurements by particle image velocimetry in Proceedings of 45th AIAA Aerospace Sciences Meeting & Exhibit* (American Institute of Aeronautics and Astronautics, Jan. 2007).
23. Raffel, M., Willert, C. E., Wereley, S. T. & Kompenhans, J. *Particle Image Velocimetry: A Practical Guide* 2nd ed. ISBN: 978-3-540-72307-3 (Springer, 2007).
24. Hain, R., Kähler, C. J. & Radespiel, R. Dynamics of laminar separation bubbles at low-Reynolds-number aerofoils. *Journal of Fluid Mechanics* **630**, 129–153 (2009).
25. Simoni, D., Lengani, D., Ubaldi, M., Zunino, P. & Dellacasagrande, M. Inspection of the dynamic properties of laminar separation bubbles: free-stream turbulence intensity effects for different Reynolds numbers. *Experiments in Fluids* **58**, 66. ISSN: 1432-1114 (May 2017).

26. Lengani, D. & Simoni, D. Recognition of coherent structures in the boundary layer of a low-pressure-turbine blade for different free-stream turbulence intensity levels. *International Journal of Heat and Fluid Flow* **54**, 1–13. ISSN: 0142-727X (2015).
27. Bragg, M. B., Khodahaust, A. & Spring, S. A. Measurements in a leading-edge separation bubble due to a simulated airfoil ice accretion. *AIAA Journal* **30** (1992).
28. Lengani, D., Simoni, D., Ubaldi, M. & Zunino, P. POD analysis of the unsteady behavior of a laminar separation bubble. *Experimental Thermal and Fluid Science* **58**, 70–79. ISSN: 0894-1777 (2014).
29. Boutillier, M. S. H. & Yarusevych, S. Parametric study of separation and transition characteristics over an airfoil at low Reynolds numbers. *Experiments in Fluids* **52**, 1491–1506 (June 2012).
30. Hudy, L. M., Naguib, A. M., Humphreys, W. M. & Bartram, S. M. *Particle image velocimetry measurements of at two/three-dimensional separating/reattaching boundary layer downstream of an axisymmetric backward facing step* in *Proceedings of 43rd AIAA Aerospace Sciences Meeting & Exhibit* (Jan. 2005).
31. Spazzini, P. G., Iuso, G., Onorato, M., Zurlo, N. & Di Cicca, G. M. Unsteady behavior of back-facing step flow. *Experiments in Fluids* **30**, 551–561 (May 2001).
32. Kiya, M. & Sasaki, K. Structure of large-scale vortices and unsteady reverse flow in the reattaching zone of a turbulent separation bubble. *Journal of Fluid Mechanics* **154**, 463–491 (1985).
33. Ansell, P. J. & Bragg, M. B. Measurement of unsteady flow reattachment on an airfoil with an ice shape. *AIAA Journal* **52**, 656–659 (2014).
34. Somers, D. M. *The S825 and S826 airfoils* (2005).
35. Hann, R. *UAV Icing: Comparison of LEWICE and FENSAP-ICE for ICE Accretion and Performance Degradation* in *Proceedings of 10th AIAA Atmospheric and Space Environments Conference conference, Atlanta* (AIAA, 2018).
36. Sirowich, L. Turbulence and the dynamics of coherent structures. Part I: Coherent structures. *Quarterly of Applied Mathematics* **45**, 561–571 (1987).
37. Meyer, K. E., Pedersen, J. M. & Özcan, O. A turbulent jet in crossflow analysed with proper orthogonal decomposition. *Journal of Fluid Mechanics* **583**, 199–227 (2007).

38. Meyer, K. E., Cavar, D. & Pedersen, J. M. *POD as tool for comparison of PIV and LES data* in *Proceedings of 7th International Symposium on Particle Image Velocimetry* (2007).

## Appendix A Experimental setup

### A.1 Design of specific experimental equipment

Fig. 3 shows the experimental setup. Equipment not present in the figure included a protection box to avoid smoke particles damaging the camera and a laser shade to comply with laser safety regulations. In addition, optical railing equipment was used to build a stand for the optics and to mount the camera to the floor of the wind tunnel.

#### A.1.1 Camera box

There were several requirements for the box intended for protecting the camera. The lid had to be transparent to allow images being captured and easy access to the camera had to be ensured. Some ventilation of the box was required to prevent the camera from over heating. The shape had to be aerodynamic, to minimise influence on the flow. The finished box is shown in Fig. A.1.



Figure A.1: Camera box before painting.

The lid was detachable, ensuring access to the camera. The large height of the box ensured that different lenses could be mounted to the camera. A tail was mounted downstream to reduce vortex shedding in the wake. The leading half cylinder was made of a pipe cut in half, the lid was acrylic, while the rest of the box was made of plywood. Manufacturing was done by the workshop employees at Department of Energy and Process Engineering at NTNU. The box was painted black ahead of the experiments, to minimise reflections in the tunnel.



Figure A.2: Laser shade.

### A.1.2 Laser shade

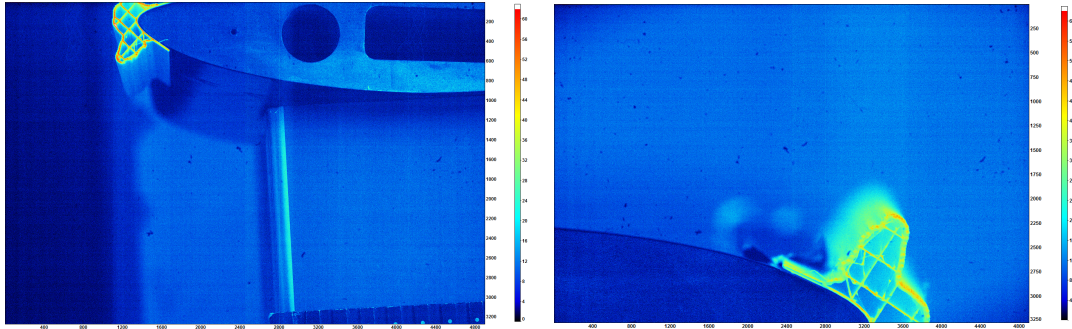
A laser shade was necessary to protect the lab from any laser light. Design requirements included a window needed to let the laser sheet enter the wind tunnel, and an entrance to allow adjustments of the optics and the optics stand. The tent was constructed by the workshop employees, and consisted of a wooden frame covered with sheets of blackout fabric. One of the sides had a double layer sheets, attached by tape, which made it possible to enter from this side. The laser shade is shown in Fig. A.2, standing beside the wind tunnel.

## A.2 Choosing field of view

The size of the field of view is determined by the focal length. Different focal lengths was considered for this work. A 200mm lens would give high resolution in the recirculating region and close to the icing geometry. A 105mm lens would give a larger field of view, allowing to see more of the separated flow for higher angles of attack, but also a lower spatial resolution. Fig. A.3 shows the size of the field of view for the two different alternatives. For the 105mm lens approximately



270mm (60%) of the airfoil chord is visible, while only 110mm (24%) is visible for the 200mm lens. Both images are taken with 0.9m distance from the airfoil to the camera, which correspond to a distance of slightly more than 1m from the floor to the measurement plane. This is a slightly shorter distance than what was used in the experiments (see Appendix A.3). A shorter focal length was not possible, as the laser would not be able to illuminate the measurement plane sufficiently for a larger field of view.



(a) 105mm.

(b) 200mm.

Figure A.3: Test images captured with the different lenses.

The experiments investigated a large range of angle of attack. It was therefore interesting to capture potential separation points and reattachment points on the airfoil surface. A larger field of view was chosen to see most of the airfoil surface. The choice of a 105mm lens did however give lower spatial resolution, including in interesting regions, as the recirculation just behind the icing geometries. The field of view is shifted upstream of the airfoil when experiments, to capture the flow in front of the leading edge. In addition, the edges of the processed material dominated by noise due to particles entering and leaving the field of view. Therefore, the results only display flow over the first 180mm (40%) of the airfoil.

### A.3 Measurement plane

As discussed in section 2.1, the measurement plane had to be located such that the effect of the boundary layer from the roof of the wind tunnel was negligible. In addition, the camera box had a major impact on the flow, so it was necessary to find how far from the box the flow was affected. Visual inspection with smoke was used to ensure that the measurement plane was far enough from the camera box to ensure the flow was approximately two dimensional.

A smoke wand was moved up and down upstream of the leading edge of

the airfoil. This was repeated both when mixed ice accretion was attached and for the clean airfoil. Angles of attack ranging from  $0^\circ$  to  $18^\circ$  was investigated. The measurement plane was set to be 1.20m above the floor of the wind tunnel. Fig. A.4 shows the visualisation at the measurement plane for mixed ice accretion at  $AoA = 0^\circ$ . The camera box is standing beside the airfoil at the approximate same location as was used in the, but is not visible in the image. Fig. A.5 indicates where on the airfoil the measurement plane was located. Note that to minimise the reflections of the laser, the icing was painted matt black before experiments were conducted.

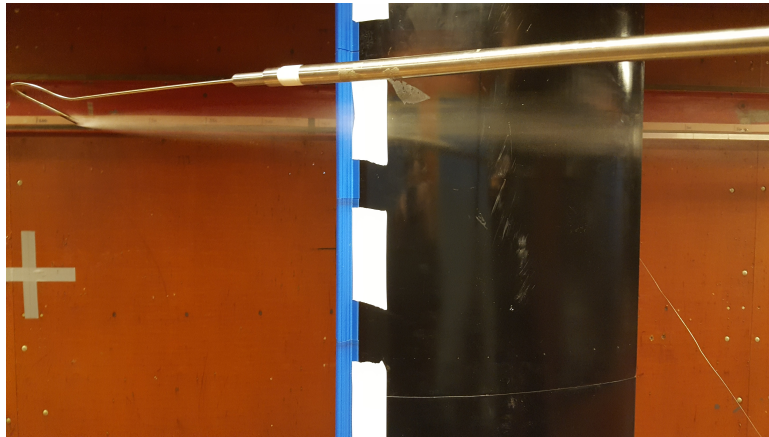


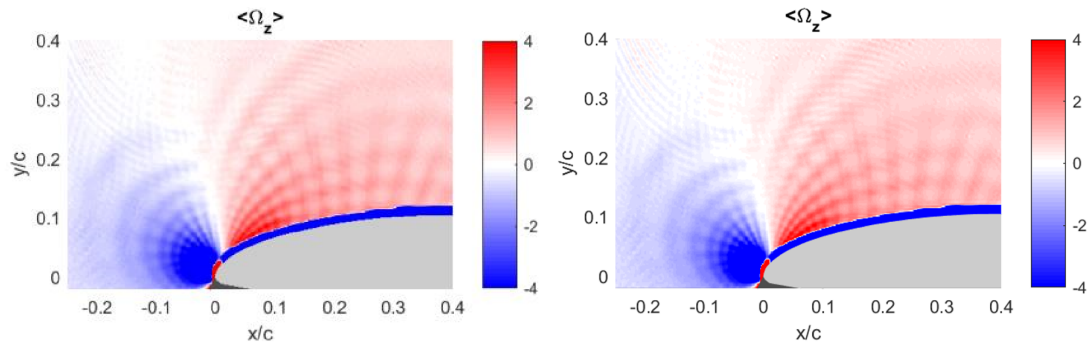
Figure A.4: Visualisation of the flow at the measurement plane, for mixed ice accretion and  $AoA = 0^\circ$ .



Figure A.5: Location of the measurement plane on the airfoil.

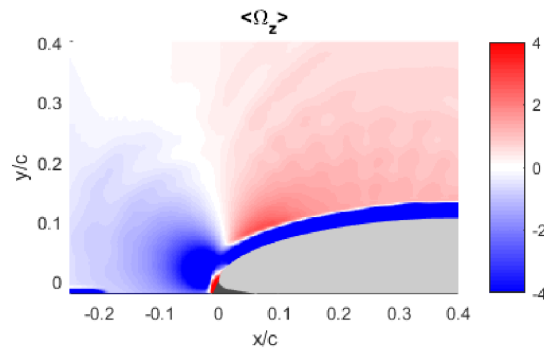
## Appendix B Selecting filter window size

Before calculating the gradients used to find vorticity and swirl, the velocity fields were filtered. This was done to smooth out any noise in the gradients. The MATLAB prefiltering function *filter2* was used for this purpose. To ensure that the size of the filter window size had no impact on the results, a comparison was made between different filter window sizes to see its effect on the mean vorticity. Window sizes of 3, 10 and 20 was used for this purpose, and calculations were performed on the clean airfoil at  $AoA = 10^\circ$ . The resulting mean vorticity fields for the three cases are shown in Fig. B.1. Window size 20 increased the thickness of the clockwise vorticity close to the airfoil. This is assumed to be due to too large filter size. There are no visible difference between using a filter size of three or ten. Three was chosen as the filter size, as there was then a good margin to any value where the window size would affect the results.



(a) Filter window size = 3 vectors.

(b) Filter window size = 10 vectors.




(c) Filter window size = 20 vectors.

Figure B.1: Mean vorticity for different filter windows.

## **Appendix C Risk assessment**

The next pages contains the signed risk assessment performed at the start of the project. It is a standard risk assessment for master students at Department of Energy and Process Engineering at NTNU.



NTNU		Risk assessment		Number		Date	
				HMSRV2603E		04.02.2011	
HSE/IKS				Prepared by		Replaces	
				HSE section		01.12.2006	
				Approved by			
				The Rector			



Unit: EPT

Date: 16.01.18



Line manager:

Participants in the identification process (including their function): Student: Magnus Kyrkjebø Vinnes, Supervisor: R. Jason Hearst  
 Short description of the main activity/main process: Master project for student Magnus Kyrkjebø Vinnes. Aerodynamics of an airfoil subjected to icing.

Signatures: Responsible supervisor: *R. J. Hearst*

Student: *Magnus Kyrkjebø Vinnes*

Activity from the identification process form	Potential undesirable incident/strain	Likelihood (1-5)	Consequence:		Risk Value (human)	Comments/status Suggested measures
			Human (A-E)	Environment (A-E)		
01 Experimental setup.	Tripping and stumbling in equipment, lights are off during experiments	4	A	A	A4	Turn on lights when needed. Use flashlight.
01 Experimental setup.	Heavy lifting, can lead to back injuries. Dropping equipment on the floor.	3	B	A	B4	Use proper lifting technique.
01 Experimental setup.	Falling ladders.	2	C	A	C2	Don't walk under ladders. Make sure ladders are secured when in use. Remove ladders when not in use.
02 PIV in vindtunnel with class IV laser.	Inproper handling of laser equipment, may lead to skin burns or ocular damage.	3	C	A	C3	Do proper laser traing courses.
02 PIV in vindtunnel with class IV laser.	Accidental exposure to laser light, due to improper alignment etc.	3	C	A	C3	Use blinds on wind tunnel windows. Cover laser beam and optics in laser shade.
02 PIV in vindtunnel with class IV laser.	Injuries due to exposure to smoke	3	A	A	A3	Water based smoke. Avoid long exposure times.

NTNU		<b>Risk assessment</b>		Prepared by	Number	Date
 HSE/KS				HSE section	HMSRV2603E	04.02.2011
				Approved by The Rector		Replaces 01.12.2006
						

**Potential undesirable incident/strain**

Identify possible incidents and conditions that may lead to situations that pose a hazard to people, the environment and any materiel/equipment involved.

**Criteria for the assessment of likelihood and consequence in relation to fieldwork**

Each activity is assessed according to a worst-case scenario. Likelihood and consequence are to be assessed separately for each potential undesirable incident. Before starting on the quantification, the participants should agree what they understand by the assessment criteria:

**Likelihood**

Minimal 1	Low 2	Medium 3	High 4	Very high 5
Once every 50 years or less	Once every 10 years or less	Once a year or less	Once a month or less	Once a week

**Consequence**

Grading	Human	Environment	Financial/material
E Very critical	May produce fatality/ies	Very prolonged, non-reversible damage	Shutdown of work >1 year.
D Critical	Permanent injury, may produce serious health damage/sickness	Prolonged damage. Long recovery time.	Shutdown of work 0.5-1 year.
C Dangerous	Serious personal injury	Minor damage. Long recovery time	Shutdown of work < 1 month
B Relatively safe	Injury that requires medical treatment	Minor damage. Short recovery time	Shutdown of work < 1week
A Safe	Injury that requires first aid	Insignificant damage. Short recovery time	Shutdown of work < 1day

The unit makes its own decision as to whether opting to fill in or not consequences for economy/materiel, for example if the unit is going to use particularly valuable equipment. It is up to the individual unit to choose the assessment criteria for this column.

**Risk = Likelihood x Consequence**

Please calculate the risk value for "Human", "Environment" and, if chosen, "Economy/materiel", separately.

**About the column "Comments/status, suggested preventative and corrective measures":**

Measures can impact on both likelihood and consequences. Prioritise measures that can prevent the incident from occurring; in other words, likelihood-reducing measures are to be prioritised above greater emergency preparedness, i.e. consequence-reducing measures.



NTNU		Risk assessment		Number		Date	
HSE/IKS				HMSRV2603E		04.02.2011	
		Prepared by		Approved by		Replaces	
		HSE section		The Reactor		01.12.2006	




from smoke machines.						Ensure no false fire alarms are triggered.
----------------------	--	--	--	--	--	--

- Likelihood, e.g.:**
1. Minimal
  2. Low
  3. Medium
  4. High
  5. Very high

- Consequence, e.g.:**
- A. Safe
  - B. Relatively safe
  - C. Dangerous
  - D. Critical
  - E. Very critical

**Risk value (each one to be estimated separately):**  
**Human = Likelihood x Human Consequence**  
**Environmental = Likelihood x Environmental consequence**  
**Financial/material = Likelihood x Consequence for Economy/material**

NTNU		Risk matrix		Date	
		HSE/KS		8 March 2010	
		prepared by		Number	
		HSE Section		HMSRV2604	
		approved by		Page	
		Rector		4 of 4	
				Replaces	
				9 February 2010	



### MATRIX FOR RISK ASSESSMENTS at NTNU

<b>CONSEQUENCE</b>		Extremely serious	E1	E2	E3	E4	E5
		Serious	D1	D2	D3	D4	D5
		Moderate	C1	C2	C3	C4	C5
		Minor	B1	B2	B3	B4	B5
		Not significant	A1	A2	A3	A4	A5
			Very low	Low	Medium	High	Very high
		<b>LIKELIHOOD</b>					

Principle for acceptance criteria. Explanation of the colours used in the risk matrix.

Colour	Description
Red	Unacceptable risk. Measures must be taken to reduce the risk.
Yellow	Assessment range. Measures must be considered.
Green	Acceptable risk Measures can be considered based on other considerations.